Three-dimensional electron microscopy uncovers mitochondrial network remodeling in residual triple negative breast cancer persisting after conventional chemotherapy treatments.

Mariah J. Berner*[1,2,3], Heather K. Beasley*[4], Benjamin Rodriguez[4], Audra Lane[1,2,3], Steven W. Wall[1,2,3], Andrea G. Marshall[4], Zer Vue[4], Larry Vang[4], Mokryun L. Baek[1,2,3,], Mason Killion[4], Faben Zeleke[4], Bryanna Shao[4], Dominque Parker[5,6], Autumn Peterson[4], Julie Sterling Rhoades[5,7], Lacey E. Dobrolecki[1,2], Amber Crabtree[4,8], Annet Kirabo[4,7], Sepiso Mansenga[4,7], Prasanna Katti[9,10,11,12], Prasanna Venkhatesh[9,10,11,12], C.V. Dash[10,11,12], Michael T. Lewis[1,2,13,14], Antentor Hinton, Jr.**[4,8,10,11,12.15], and Gloria V. Echeverria**[1,2,3,13,14,16]

*Co-first authors

**Co-corresponding authors

[1]Lester and Sue Smith Breast Cancer, Baylor College of Medicine, Houston, TX, USA

[2]Dan L Duncan Comprehensive Cancer Center, Baylor College of Medicine, Houston, TX, USA

[3]Department of Medicine, Baylor College of Medicine, Houston, TX, USA

[4]Department of Molecular Physiology and Biophysics, Vanderbilt University, Nashville, TN, USA.

[5]Department of Veterans Affairs, Tennessee Valley Healthcare System, Nashville, TN, USA

[6]Program in Cancer Biology, Vanderbilt University School of Medicine, Nashville, TN, USA

[7]Department of Medicine, Division of Clinical Pharmacology, Vanderbilt University Medical Center, Nashville, TN, USA

[8]First Center for Autism & Innovation, Vanderbilt University, Nashville, TN, USA

[9]Department of Biology, Indian Institute of Science Education and Research (IISER), Tirupati, AP, India

[10]The Center for AIDS Health Disparities Research, Meharry Medical College, Nashville, TN, USA

[11]Department of Microbiology, Immunology, and Physiology, Meharry Medical College, Nashville, TN, USA

[12]Department of Biochemistry, Cancer Biology, Pharmacology and Neuroscience, Meharry Medical College, Nashville, TN, USA

[13]Department of Molecular and Cellular Biology, Baylor College of Medicine, Houston, TX, USA

27 [14]Department of Radiology, Baylor College of Medicine, Houston, TX, USA

28 [15]Department of Medicine, Division of Cardiology, Vanderbilt University Medical Center, Nashville, TN, USA

29 [16]Department of Radiation Oncology, Baylor College of Medicine, Houston, TX, USA

30

31 **Correspondence**: Gloria Echeverria (gloria.echeverria@bcm.edu) and Antentor Hinton, Jr.

32 (antentor.o.hinton.jr@vanderbilt.edu)

33

34 **DISCLOSURES**

35 MTL is a founder and limited partner in StemMed Ltd. and a manager in StemMed Holdings, its general partner.
36 He is a founder and equity stakeholder in Tvardi Therapeutics Inc. Some PDX models, none of which are
37 included in this study, are exclusively licensed to StemMed Ltd., resulting in royalty income to MTL. LED is a
38 compensated employee of StemMed Ltd. Some PDX models, none of which are included in this study, are
39 exclusively licensed to StemMed Ltd., resulting in royalty income to LED. GVE previously received sponsored
40 research funding from Chimerix, Inc and receives experimental compounds from the Lead Discovery Center of
41 Germany and Jazz Pharmaceuticals. All other authors have nothing to disclose.

42

43 **ABSTRACT**

44 Mitochondria are hubs of metabolism and signaling, playing crucial roles in tumorigenesis, therapeutic
45 resistance, and metastasis in many types of cancer. Various laboratory models of cancer demonstrate the
46 extraordinary dynamics of mitochondrial structure, but little is known about the full extent of the complexity of the
47 mitochondrial network, nor its regulation upon exposure to therapeutic stressors. We previously demonstrated
48 the importance of mitochondrial structure and oxidative phosphorylation in the survival of chemotherapy-
49 refractory triple negative breast cancer (TNBC) cells. As TNBC is a highly aggressive breast cancer subtype with
50 few targeted therapy options, conventional chemotherapies remain the backbone of TNBC treatment.
51 Unfortunately, approximately 45% of TNBC patients retain substantial residual tumor burden following
52 chemotherapy, associated with abysmal prognoses. Herein we present the first three-dimensional analysis of
53 mitochondrial networks in human tumor tissues. Use of two experimentally tractable orthotopic patient-derived

xenograft (PDX) models TNBC enabled us to conduct longitudinal analyses to construct mitochondrial networks in treatment-naïve and residual tumors persisting after exposure to a variety of conventional chemotherapies. Further, we modeled lipid droplet (LD) structures and their physical contacts with mitochondria. In total, we reconstructed 3,750 mitochondria and 800 LDs in three dimensions using serial block-face scanning electron microscopy (SBF-SEM), providing unprecedented insights into the complexity and intra-tumoral heterogeneity of mitochondria in TNBC. Both carboplatin (CRB) and docetaxel (DTX) chemotherapies produced residual tumors that harbored mitochondria with significantly increased areas, volumes, and perimeters in both PDX models. Additionally, treatment with the conventional combinations DTX plus CRB or Adriamycin plus cyclophosphamide (AC), led to reduced mitochondrial branching and elongation. In contrast, DTX or CRB alone elicited model-specific changes in mitochondrial complexity. Further, the extensive intra-tumoral heterogeneity of mitochondrial structure in untreated PDX tumors significantly decreased in residual tumors. Analyses of LDs revealed significant and consistent elevation of the number and physical proximity of MLCs in residual tumors, congruent with our previous studies providing evidence for transcriptomic and proteomic rewiring of lipid metabolism in residual TNBC. These results highlight the potential for structure-based monitoring of chemotherapeutic metabolic reprogramming and suggest unique molecular mechanisms that may underlie chemoresistance in TNBC. Furthermore, our findings provide novel insights into a new type of intratumoral heterogeneity, that of mitochondrial intratumoral heterogeneity, which complements our understanding of the genomic, epigenomic, transcriptomic, and proteomic complexity of TNBC.

INTRODUCTION

Triple negative breast cancer (TNBC), an aggressive subtype of breast cancer, comprises approximately 15% of breast cancer cases[1]. Because TNBCs do not express estrogen or progesterone receptors or overexpress the human epidermal growth factor receptor 2, there are limited targeted therapies for this subtype[1,2]. Most patients with TNBC receive pre-surgical neoadjuvant chemotherapy (NACT) typically including several conventional chemotherapeutic agents given in simultaneous and/or sequential combinations. NACT now also consists of the immunotherapy agent Programmed Cell Death 1 (PD-1) inhibitor, with a marginal but statistically significant improvement in response rate[3]. Conventional chemotherapies typically include DNA-

81 damaging agents (*e.g.*, Adriamycin, cyclophosphamide, carboplatin) and microtubule disrupting taxanes (*e.g.,*
82 docetaxel, paclitaxel). As there is no single accepted standard NACT regimen for TNBC, a variety of regimens
83 are used throughout the United States and worldwide[4]. Pathology evaluation of the resected surgical specimen
84 assesses residual cancer burden (RCB) following NACT. Unfortunately, approximately 45% of TNBC patients
85 retain substantial RCB after NACT, which is strongly associated with high rates of metastatic relapse and
86 mortality[5,6]. Thus, understanding the molecular features of residual tumor cells that survive chemotherapeutic
87 regimens is key to developing novel strategies to combat residual disease.
88
89 Mitochondria adapt to meet the cell's energetic and signaling demands in response to exogenous stressors,
90 in part through mitochondrial structural rearrangements and communication with other organelles[7]. In the context
91 of cancer, metabolic adaptations orchestrated by mitochondria can encompass oxidative phosphorylation
92 (oxphos), glycolysis, reactive oxygen species (ROS), nucleotide synthesis, and fatty acid oxidation as we
93 recently reviewed[8]. The interplay between mitochondrial fission and fusion, dictating mitochondrial structure, has
94 been studied in relation to cancer therapy resistance and metastasis. For TNBC, mitochondrial structure
95 dynamics play a role in metastatic phenotypes, although the findings seem to be context-dependent[9,10], as well
96 as resistance to standard chemotherapies[11]. Importantly, we demonstrated that chemotherapy-induced
97 adaptations in mitochondrial structure and function produced a new therapeutic dependency for residual TNBC,
98 allowing us to delay tumor regrowth by inhibiting mitochondrial fusion or by direct inhibition of Complex I[11-13].
99 Complementing our TNBC work[11] with the first-generation OPA1 inhibitor MYLS22[14], an optimized compound
100 was recently described[15], further establishing the promise of inhibiting mitochondrial structure dynamics as an
101 anticancer strategy. These studies highlight the growing interest in translating mitochondrial structure
102 perturbations to the clinic for cancer patients.
103 Serial block-face scanning electron microscopy (SBF-SEM) was first developed in 2004 by Denk and
104 Horstmann to study mitochondrial structure and location within the neuron[16,17]. This state of the art imaging
105 method produces high-resolution micrographs that capture subcellular ultrastructural features through three-
106 dimensional (3D) rendering that, unlike other volumetric electron microscopy techniques, provides large x- and
107 y-axis ranges[18-20]. These visualizations of changes in mitochondrial morphology, orientation, configuration, size,

108 and shape provide insights into mitochondrial physiology and function, important for physiology and disease[21-
109 24]. We and others have shown that using 2D transmission electron microscopy (TEM) to characterize
110 mitochondrial structures in breast cancer provides useful, albeit limited, insights into the extent of the
111 mitochondrial network[10,11,25,26]. Previous SBF-SEM studies of mitochondria demonstrated dynamic 3D structures
112 and networks associated with skeletal muscle physiology[27], aging[28-30], and tumor cell culture methodologies[31].
113 Of note, a recent non-small cell lung cancer study employed genetically engineered mouse models to
114 demonstrate that 3D mitochondrial structure was spatially heterogeneous within tumor cells and functionally
115 affected mitochondrial respiration[32].

116 The nature of 3D mitochondrial networks in human cancer tissues remains currently undocumented. In fact,
117 there are no published SBF-SEM mitochondria analyses of any human cancer tissues. Further, this approach
118 has not been used to address biologically important transitions during cancer, namely response to therapeutic
119 stressors. To address these knowledge gaps in light of our prior work demonstrating the importance of
120 mitochondrial structure and oxphos for TNBC chemoresistance, we used SBF-SEM to determine 3D
121 mitochondrial networks in two experimentally tractable orthotopic PDX models of TNBC. PDXs provide valuable
122 models for longitudinal studies to evaluate chemotherapy response as they effectively recapitulate the molecular
123 features and heterogeneity observed in human TNBC[33-37]. Our longitudinal analyses enabled us to compare
124 residual tumors surviving exposure to a variety of conventional chemotherapies to their treatment-naïve
125 counterparts. We found significant changes in mitochondrial shape, size, branching, complexity, and contacts
126 with lipid droplets (LDs) in residual tumors compared to treatment-naïve tumors. Further, we found striking
127 intratumoral heterogeneity (ITH) of mitochondria (mITH) within individual tumors that was most pronounced in
128 the treatment-naïve tumor. This finding highlights the incredible complexity within individual TNBC tumors and
129 reaffirms the extensive ITH that has been thoroughly documented at the genomic, transcriptomic, epigenetic,
130 and proteomic levels[38,39]. Together, these results demonstrate the incredible adaptability of mitochondrial 3D
131 structure as TNBCs are exposed to conventional chemotherapies. We and others have shown the promise of
132 mitochondrial interventions for anticancer therapy, and these results lay the groundwork for structure-based
133 monitoring of treatment responses and anti-mitochondria therapeutic efficacy in TNBC.
134

135 **METHODS**

136 **Patient-derived xenograft mouse studies**

137 Animal studies were conducted in accordance with the National Institutes of Health *Guide for the Care and Use*
138 *of Laboratory Animals* with approval of the BCM IACUC under protocol AN-8243 and AN-2289. Mice were
139 ethically euthanized as recommended by the Association for Assessment and Accreditation of Laboratory Animal
140 Care. The PIM001-P PDX model was originally obtained from the University of Texas MD Anderson Cancer
141 Center, where it was generated and characterized and was then propagated at BCM as described previously[13,35].
142 Briefly, cryo-preserved PDX cells were suspended as a 1:1 volume mixture in a total of 20 µl of complete cell
143 growth medium (Dulbecco's modified Eagle's medium:F12, Cytiva HyClone, SH30023.01) supplemented with
144 5% fetal bovine serum and Matrigel (Corning, 354234). 5.0×10^5 viable tumor cells were injected unilaterally into
145 the fourth mammary fat pads of 5- to 8-week-old female Nod-Rag-Gamma mice (NRG*, Nod.Cg-Rag1*^{tm1Mom}/
146 *IL2rg*^{tm1wjl}*/SzJ*, The Jackson Laboratory). The WHIM14 PDX model mice were implanted unilaterally as 1x1 tumor
147 chunks into the fourth mammary fat pad by the BCM Patient-derived Xenograft Core as described previously[40].
148

149 To validate PDX models, the Cytogenetics and Cell Authentication Core at MD Anderson Cancer Center
150 performed short-tandem repeat (STR) DNA fingerprinting on DNA extracted from PDX tumors. The Promega 16
151 High Sensitivity STR Kit (Catalog # DC2100) was used for fingerprinting analysis, and profiles were compared
152 to online databases (DSMZ/ ATCC/ JCRB/ RIKEN).
153

154 Mouse body weights and tumor volumes, measured using digital calipers, were recorded twice weekly for the
155 duration of the experiment. When mammary tumors reached an average size of 150 mm^3, mice were randomized
156 into five treatment groups (n = 6 mice per group) to monitor tumor responses and collect samples for molecular
157 analyses. For the treatment-naïve group, the tumors were harvested at 150 mm^3 without any treatment. Mice in
158 the Adriamycin plus cyclophosphamide (AC) treatment group received one dose of Adriamycin and
159 cyclophosphamide every three weeks for a total of three doses. Adriamycin (doxorubicin, ChemieTek, CT-
160 DOXO) was solubilized in sterile water immediately before administration and protected from light prior to
161 intraperitoneal (i.p.) injection at a dose of 0.5 mg/kg. Cyclophosphamide (Sandoz, 0781-3244-94) was solubilized

162 in sterile water immediately prior to administration via i.p. injection at 50 mg/kg. Mice in the docetaxel (DTX), the
163 carboplatin (CRB), and the docetaxel plus carboplatin combination (DTX+CRB) treatment groups received
164 weekly doses for three weeks. Docetaxel (Hospira, 0409-0201-10) was supplied in a solution of polysorbate
165 80NF, 4 mg anhydrous citric acid USP, 23% v/v dehydrated alcohol USP, q.s. with polyethylene glycol 300 NF
166 at 20 mg/kg. DTX was administered by i.p. injection at a dose volume of 2 ml/kg. Carboplatin (TEVA
167 Pharmaceuticals, 0703-4248-01) was supplied at 10 mg/ml in water for i.p. injection at 50 mg/kg at a dose volume
168 of 5 ml/kg. For the DTX+CRB treatment group, each compound was administered consecutively by i.p. injection.
169 For each group of the PIM001-P PDX model, residual tumors were harvested one complete cycle after the third
170 dose of chemotherapy (i.e., a total of 28 days after the start of treatment for DTX, CRB, DTX+CRB, and 63 days
171 after the start of treatment for AC). For each group of the WHIM14 PDX model, residual tumors were harvested
172 when they had regressed in size by 40% because insufficient tumor material would be available for analyses
173 after ~1.5 weeks of starting treatment in this model due to its rapid regression.
174

175 **Formalin-fixed paraffin-embedded (FFPE) tissue staining**

176 After harvesting the tumors, we immediately fixed tumor fragments in formalin (Sigma HT501128-4L) for 48
177 hours at room temperature on a rocker, washed them with 1× phosphate-buffered saline, and stored them in
178 70% ethanol at 4 °C until they were submitted to the BCM Pathology Core and Lab to be processed into paraffin
179 blocks, cut into 3um sections, and stained with hematoxylin and eosin (H&E). Immunohistochemical staining with
180 antibodies against Ki67 (Dako catalog #M7240, 1:200), Ku80 (CST 2180, 1:100), and human-specific
181 mitochondria (Abcam 92824, 1:1,000) was conducted as described previously[13].
182

183 **SBF-SEM sample processing**

184 Tumors were harvested from the mammary gland immediately after the mice were euthanized and immediately
185 placed in fixative. A tumor slice ~1 mm thick was placed into 1 ml of fixative (2% paraformaldehyde + 2%
186 glutaraldehyde in 0.15 M cacodylate buffer) and stored at 4°C until they were sent to the Mayo Microscopy and
187 Cell Analysis Core for processing and imaging. Tissue samples for SBF-SEM were prepared using a modified
188 procedure[23,41]. Briefly, fixed tissue was rinsed in 0.1 M cacodylate buffer and placed in 2% osmium tetroxide +

189 1.5% potassium ferracyanide in 0.1 M cacodylate, washed with nH_2O (MilliQ water), incubated at 50°C in 1%
190 thiocarbohydrazide, incubated again in 2% osmium tetroxide in nH_2O, rinsed in nH_2O and placed in 2% uranyl
191 acetate overnight. The next day, the tissue was rinsed again in nH_2O, incubated with Walton's lead aspartate,
192 dehydrated through an ethanol series, and embedded in Embed 812 resin. To prepare embedded tissue for
193 placement into the SBF-SEM, a ~1.0 mm^3 piece was trimmed of excess resin and mounted on an 8 mm aluminum
194 stub using silver epoxy Epo-Tek (EMS, Hatfield, PA). The mounted sample was then carefully trimmed into a
195 smaller ~0.5 mm^3 tower using a Diatome diamond trimming tool (EMS, Hatfield, PA) and vacuum sputter-coated
196 with gold-palladium to help dissipate any charge. Sectioning and imaging of the sample were performed using a
197 VolumeScope 2 SEM™ (Thermo Fisher Scientific, Waltham, MA). Imaging was performed under low
198 vacuum/water vapor conditions with a starting energy of 3.0 keV and a beam current of 0.10 nA. Sections of 50
199 nm thickness were cut, providing a final image spatial resolution of either 15 nm × 15 nm × 50 nm or 10 nm × 10
200 nm × 50 nm.
201
202 **SBF-SEM data analysis**
203 Image analyses, including registration, volume rendering, and visualization, were performed using Amira
204 (Thermo Fisher) software packages. The selection criteria for a region of interest (ROI) included tumor regions
205 and excluded necrotic and extracellular matrix regions. A minimum of three ROIs were selected per sample. For
206 each sample, images were collected from at least 300 serial sections that were then stacked, aligned, and
207 visualized using Amira to make videos and quantify volumetric structures. A random number generator was used
208 to select 350 segmented mitochondria for each tumor of the PIM001-P for the final analysis. See Supplementary
209 Table 1 for the specific number of mitochondria segmented per ROI and those selected for final analysis of the
210 PIM001-P model. With the WHIM14 model, two ROIs were selected per sample, and a random number generator
211 was used to select 500 segmented mitochondria for each WHIM14 tumor (supplementary Table 2). Additionally,
212 for the WHIM14 model, we segmented a total of 200 lipid droplets from the two selected ROIs to analyze the
213 mitochondria-lipid droplet interactions further (supplementary Table 3). Previously defined protocols using Amira
214 software provide a workflow for 3D reconstructed organelles by manual or semi-automated segmentation[19,20].
215 Amira provides parameters for quantifying 3D structures, many of which are included in the software, such as

volume and surface area. We have added sphericity, which is measured through the Feret's Diameter. Feret's diameter refers to the distance between any two most distant points in a 3D object. Sphericity refers to the adherence of the object to that of a sphere and is calculated by the equation $(\pi^{1/3}(6V)^{2/3})/SA$, where V is the volume of the object, and SA is the surface area of the object. We also quantified the mitochondrial complexity index, calculated by the equation $SA^3/16\pi^2V^2$, and the mitochondrial branching index, which calculates the relative branching between the transverse and longitudinal mitochondrial orientations[24].

Statistical analyses

We evaluated the means for each measurement between treatment groups by the Mann–Whitney U test followed by the Holm method of p-value adjustment[42-44]. We performed Bartlett's test followed by pairwise F-tests to determine whether the variance of each measurement differed between treatment groups using R 4.1.0 (R Core Team, 2023) and the *stats* package (base statistical package in R)[45]. Bartlett's test assesses whether all the treatment groups have the same variance. A p-value less than 0.05 for a given measurement by Bartlett's test indicates that some of the treatment groups have different variances for that measurement. To identify which treatment groups differed, we then conducted a two-tailed F-test on each possible pairwise comparison between treatment groups. In a two-tailed F test, the F value is defined as the quotient of the variance of one group divided by the variance of the other. This F value is used to test whether the variance in the numerator equals that in the denominator. For a given F test, a p-value was determined by taking the area under the F distribution beyond that test's F value and then subtracting that area from 1. Once all possible comparisons had been made for a measurement, the p-values for that measurement were adjusted by the Holm method to account for multiple comparisons.

RESULTS

Various conventional chemotherapies elicited drastic tumor regression followed by regrowth in TNBC PDX models.

242 To model the residual tumor state, which we previously showed exhibits increased OXPHOS and
243 mitochondrial dependence, we treated the orthotopic PIM001-P[13,35] PDX model with conventional chemotherapy
244 agents administered either individually or in combination: AC, docetaxel (DTX), carboplatin (CRB), or DTX+CRB
245 (Fig. 1a). Interestingly, we found that DTX, CRB, and DTX+CRB all elicited similar responses as did AC,
246 congruent with our previous reports: initially drastic tumor regression to a 'residual' tumor, maintenance of a
247 residual tumor for weeks to months, then regrowth of the tumor. We next tested an additional orthotopic PDX
248 model, WHIM14[46], with DTX, CRB, or DTX+CRB, similarly demonstrating tumor regression followed by regrowth
249 (Fig. S1a). Both PIM001-P and WHIM14 are models of aggressive TNBC: PIM001-P was derived from the
250 primary tumor of a treatment-naïve TNBC patient diagnosed with *de novo* metastasis, who received gemcitabine
251 and paclitaxel had an overall survival of four months[13,35]. WHIM14 was generated from a chest wall metastasis
252 of a heavily pre-treated TNBC patient who continued to receive additional therapies, with an overall survival of
253 37 months[46].

254 Treatment-naïve (TN) tumors were collected from a subset of mice for each model when tumors reached
255 approximately 150 mm^3. For PIM001-P, after three treatment cycles, residual tumors were harvested on the day
256 that the fourth cycle would have begun. These residual tumors showed an average decrease in tumor volume of
257 53.6% (DTX, 52.9%; CRB, 61.0%; DTX+CRB, 61.5%; and AC, 34.0%) (Fig. 1b). WHIM14 regressed more rapidly
258 and extensively, with an average reduction in tumor volume of 60% after only one cycle of treatment (Fig. S1a).
259 Accordingly, 'residual' tumors in this model were harvested relatively early, when volumes had decreased to
260 approximately 40% of the initial volume after the first cycle. The mice remaining in each treatment arm for
261 regrowth monitoring received three additional cycles (four in total) of chemotherapy. At the indicated time points,
262 three to four mice were euthanized, and their residual tumors were collected, and from these, one tumor was
263 randomly selected for SBF-SEM and conventional histology analyses. The remaining mice were monitored for
264 relapse and then euthanized once tumors regrew to at least 100% of their original volume. In three cases, mice
265 succumbed to drug-related toxicities, all within the DTX+CRB group. We were unable to assess the regrowth in
266 PIM001-P after four cycles of DTX+CRB. To address this, we conducted a follow-up study with a single cycle of
267 treatment, demonstrating robust regrowth after the initial regression (Fig. S2a).

268 H&E staining of TN FFPE tumor sections revealed poorly differentiated cellular architecture with
269 abundant mitotic figures. All residual tumors in chemotherapy treatment groups exhibited extensive desmoplasia
270 with significant tumor cell pleomorphism, including atypical and enlarged nuclear and cytoplasmic sizes and
271 shapes, pronounced nucleoli, and areas of necrosis, consistent with chemotherapy-induced cytological changes
272 observed previously in PDXs and in patients[13,47] (Fig 1c & S1b). Notably, residual tumors retained cycling Ki67
273 positive cells (Fig 1c), in line with our prior AC study in PIM001-P[13]. Ku80 staining, used to distinguish human
274 tumor cells from mouse stromal cells, revealed an abundant stromal component in all residual tumors (Fig. 1c),
275 as previously reported with AC treatment[13]. Staining with an antibody specific for human mitochondria,
276 demonstrated increased mitochondrial content in residual tumor cells compared to TN cells, consistent with our
277 prior finding in AC-treated residual tumors (Fig. 1c)[13]. In summary, various conventional chemotherapies induced
278 tumor regression in both PIM001-P and WHIM14. The residual tumors exhibited regrowth capacity, aberrant
279 histology architecture, and increased mitochondrial content in the tumor cell compartment.
280

281 **3D rendering of mitochondria by SBF-SEM revealed residual tumor mitochondria had increased volume,**
282 **area, and perimeter relative to TN.**

283 From each treatment group, we selected one representative tumor with a volume close to the group's
284 mean to generate blocks for SBF-SEM. Electron micrographs were acquired at either 15 nm × 15 nm × 50 nm
285 or 10 nm × 10 nm × 50 nm resolution with a minimum of three ROIs, each with 300 slices, per tumor. ROIs were
286 inspected prior to imaging to avoid necrotic and stroma-rich regions. Mitochondria segmentation was conducted
287 across different areas of each orthogonal (ortho) slice (Fig. 2a-e; Fig. S3a-d) to capture spatial heterogeneity
288 within tumors. Each individual segmented mitochondrion used for final analyses was manually inspected to
289 confirm complete segmentation (*i.e.,* not missing a slice) (Fig. 2a'-e', Fig. S3a'-d'). From each tumor, we
290 randomly selected 350 mitochondria from PIM001-P (Fig. 2a'-e'') and 500 mitochondria from WHIM14 (Fig.
291 S3a''-d'') for morphometric analyses from a minimum of three or two ROIs, respectively. For each mitochondrion,
292 we computed area, volume, and perimeter as described previously[19,20,27].

293 We compared the mean values of each mitochondrial feature between tumors. To assess differences in
294 these means between treatment groups, we performed Mann–Whitney U tests, as q–q plots indicated that

295 mitochondrial features were not normally distributed, precluding the use of ANOVA (Fig. S4). In both PDX
296 models, DTX and CRB residual tumors had significantly increased mitochondrial area, volume, and perimeter
297 compared to treatment-naïve tumors (Fig 2f-h, S3e-g). This effect was also observed following DTX+CRB
298 combination treatment in WHIM14. Although no significant changes were detected in PIM001-P with the
299 DTX+CRB combination, the median mitochondrial area and volumes were elevated relative to TN. In contrast,
300 AC treated PIM001-P residual tumors exhibited no change in mitochondrial area, perimeter, or volume relative
301 to TN.

302 TNBC is characterized by extensive intratumoral heterogeneity at the genomic[48-50], epigenetic[51],
303 transcriptomic[52], cell type[53], spatial[54,55], and proteomic[56,57] levels. Here we observed substantial intra-tumoral
304 mitochondrial heterogeneity (mITH), which was more pronounced in PIM001-P than in WHIM14. To quantify this,
305 we generated density plots and computed variances of each metric in each sample. The density plots confirmed
306 the aforementioned increases in area, volume, and perimeter and further illustrated a broader distribution of
307 mitochondrial features in TN tumors compared to most residual tumors (Fig. S5-8). Notably, variance was
308 significantly reduced in all residual tumors compared to TN in both models, with the exception of mitochondrial
309 volume in DTX-treated WHIM14 (Fig S9 & S10). This reduction in variance was particularly striking in PIM001-
310 P (Fig S9). Together, these findings demonstrate that DTX, CRB, and DTX+CRB elevated mitochondrial area,
311 volume, and perimeter in both PDX models while simultaneously inducing a significant reduction in mITH.

312

313 **Residual tumors harbored mitochondria with greater complexity.**

314 We next analyzed mitochondrial elongation and branching. Sphericity scores (ranging from 0 to 1, with 1
315 representing a perfect sphere) were calculated, revealing significant yet minor changes in residual tumors
316 relative to TN tumors. (Fig. 3a&b, Fig. S11a&b). Specifically, mitochondria in all residual WHIM14 tumors, as
317 well as those in the DTX+CRB and AC-treated residual PIM001-P tumors, showed increased sphericity
318 (significantly, or trending towards significance). By contrast, mitochondria in PIM001-P residual tumors following
319 DTX and CRB treatment had significantly decreased sphericity, consistent with elongation. To further evaluate
320 elongation, we computed the mitochondrial branching index (MBI), a conventional metric that reflects the
321 directionality of elongation[27]. MBI is defined as the ratio of the longest point in the transverse direction (in this

322 case, width) to the longest point in the longitudinal direction (length) (Fig. S12a). MBI results matched the
323 aforementioned sphericity results (Fig. S12b&c). To assess mitochondrial branching and structural complexity,
324 we calculated the mitochondrial complexity index (MCI)[27], which incorporates both 3D volume and surface area.
325 Conceptually, a more branched mitochondrion would have a larger surface area than a less branched one of
326 equal volume, yielding a higher MCI. Residual tumor mitochondria in WHIM14, as well as those in the DTX+CRB
327 and AC-treated PIM001-P residual tumors, showed significant decreases in MCI. In contrast, mitochondria from
328 PIM001-P tumors treated with single agent DTX or CRB treatment increased MCI (Fig. 3c & S11c), consistent
329 with greater branching and/or elongation.

330 We next assessed mitochondrial shape using MCI, MBI, and sphericity. Variance analyses revealed a
331 consistent and significant reduction in nearly all metrics in all residual tumors relative to TN (Fig. S9 & S10). As
332 a result of the extensive mITH, we displayed a representative subset of the top, middle, and bottom 10% of
333 mitochondria based on volume within each tumor. To visualize the mitochondrial structural diversity, we
334 performed mito-otyping[27], a karyotype-like arrangement of mitochondria to visualize complexity relative to
335 volume (Fig. 4a, Fig. S13a). Consistent with the quantitative data, mito-otyping revealed substantial mITH in all
336 tumors, along with significant shifts in the size and complexity of mitochondria following chemotherapy. Overall,
337 these findings suggest that mitochondria tend to become less branched and/or elongated after treatment with
338 DTX+CRB or AC. In contrast, single-agent DTX or CRB treatment produced divergent phenotypes between the
339 two PDX models. As with the other mitochondrial features, all treatments elicited a substantial reduction in mITH.
340

341 **Mitochondrial-lipid droplet contacts increase in frequency while decrease in size upon chemotherapy**

342 Lastly, while segmenting mitochondria in the second PDX model, WHIM14, we observed a striking
343 abundance of lipid droplets (LDs). Since mitochondria do not function independently but instead interact with
344 other organelles to facilitate the exchange of biomolecules, we extended our characterization to model 3D
345 structures of mitochondrial-LD contact (MLC) sites. To this end, we first segmented 200 lipid droplets from each
346 WHIM14 tumor (supplementary Table 3). We found that volume, area, and perimeter of lipid droplets increased
347 in residual tumors persisting after single-agent chemotherapy treatments compared to the TN tumor (Fig. S14).
348 Of the 500 segmented mitochondria and 200 segmented LDs in each WHIM14 tumor, we found 105 MLCs in

349 the TN tumor, 188 in the DTX tumor, 137 in the CRB tumor, and 167 in the DTX+CRB tumor. Representative 3D
350 MLCs are shown from the side, top, and zoomed top views (Fig. 5a-d''). When considering the proportion of the
351 mitochondria in contact with LDs, we observed that all chemotherapy-treated groups have increased MLCs
352 compared to the TN (Fig. 5e). We then assessed the size of these contacts by evaluating their surface area and
353 volume from the two ROIs selected (Fig. 5f & g). For both ROIs, the MLC surface areas and volumes, per the
354 total sum of the mitochondrial surface areas or volumes, were substantially lower in residual tumors compared
355 to the TN tumor (Fig. 5h & i). Taken together, these analyses demonstrate that although chemotherapy increased
356 the size of LDs and the number of mitochondria–lipid droplet contacts in residual tumors compared to TN, the
357 surface area and volume of the MLCs was markedly reduced. These results suggest that chemotherapy
358 substantially altered crosstalk between LDs and mitochondria, simultaneously increasing the likelihood of contact
359 formation while limiting the physical size of the interactions.

360 It is important to note that reduced surface area or volume of MLCs has been shown to reflect increased
361 exchange of biomolecules such as ATP and fatty acids between mitochondria and LDs, potentially through closer
362 physical connection[58,5958]. In alignment with this, we previously published transcriptomic rewiring of the fatty acid
363 metabolism pathway in residual PDX tumors persisting after AC treatment[13]. Further, proteogenomic analyses
364 of 16 pairs of matched human TNBC biopsies prior to and following exposure to DTX+CRB revealed significant
365 elevation of fatty acid metabolism pathways[41]. Together, these findings underscore the importance of future
366 functional investigations into the role of mitochondria-lipid crosstalk in TNBC.

367

368 **DISCUSSION**

369 Although chemotherapy is the backbone of TNBC treatment, there is no clear molecular rationale for
370 choosing specific chemotherapeutic regimens and little understanding of the dependencies of chemo-refractory
371 TNBC cells. While efforts have been made to identify molecular features that inform targeted treatments-such
372 as with PARP inhibitors[2] or immune checkpoint inhibitors[60], poor understanding of how to select the most
373 effective chemotherapies based on tumor molecular features remains. Thus, elucidating the biological properties
374 of tumor cells that survive NACT is critically important for overcoming chemoresistance and improving overall

375 survival for those 45% of TNBC patients whose tumors persist despite months of intensive, harsh chemotherapy
376 treatments.

377 We previously established the functional importance of mitochondrial structure in supporting oxphos in
378 chemoresistant TNBC. Furthermore, we demonstrated that inhibition of OXPHOS[13] or of mitochondrial fusion[11]
379 in residual tumors persisting after chemotherapy significantly prolonged tumor control. Our study provides
380 evidence that chemotherapy substantially alters the mitochondrial network in residual tumors across two unique
381 PDX models treated with several conventional chemotherapeutic agents.

382 We observed greater volume, area, and perimeter of mitochondria in residual tumors after chemotherapy
383 compared to treatment-naïve tumors in both TNBC PDX models. This may support increased metabolic capacity,
384 as our previous study of TNBC demonstrated that mitochondrial elongation enhanced OXPHOS in residual
385 tumors[11]. However, distinguishing the relative contributions of mitochondrial volume/area and the actual shape
386 (elongated, spherical) remains a challenge in the mitochondrial structure field and is an active area of
387 investigation. Thus, it is not immediately clear how the mitochondrial structures observed here may impact
388 mitochondrial functions such as OXPHOS, redox regulation, anaplerosis, apoptosis, and cellular signaling.
389 Mitochondrial dysfunction—an intricate condition with a wide ranging consequences—cannot be definitively
390 inferred from the 3D mitochondrial structure alone. Nevertheless, given the importance of understanding
391 mitochondrial dynamics in TNBC, the unique mitochondrial morphologies we observed in this study merit further
392 functional investigations that may lead to therapeutic insights.

393 Mitochondria also interact and communicate with multiple organelles, such as the endoplasmic reticulum
394 (ER). In fact, mitochondrial fission occurs at mitochondria-ER contact sites[21,61,62]. Mitochondria further engage
395 with LDs, the nucleus, the Golgi, and lysosomes[22,63-66]. However, the prevalence and significance of these
396 mitochondria—organelle contact sites remain hardly addressed in cancer and are practically unexplored in
397 TNBC[67]. We observed an increase in mitochondrial surface area in residual tumors after chemotherapy,
398 potentially creating more opportunities for organelle interactions. Indeed, one of our models exhibited marked
399 levels of LDs, and we found that MLCs increased in all chemotherapy-treated tumors compared to the TN tumor.
400 However, MLC size, measured by surface area and volume, was reduced in the residual tumors relative to TN.
401 This suggests that while chemotherapy increases the frequency of MLCs, their smaller size may reflect tighter

402 junctions between mitochondria and LDs[68]. LDs are evolutionarily conserved organelles known to support
403 lipogenesis and triacyl glyceride synthesis[58,59], while also storing and releasing lipids to meet the energetic
404 demands of the cell in coordination with mitochondria[69,70]. Notably, peridroplet mitochondra, a subpopulation of
405 the mitochondria tightly associated with LDs, are reported to increase under stress and display heightened
406 activity. These mitochondria exhibit enhanced TCA cycling, electron transport chain complex activity, oxygen
407 consumption rate, and ATP synthesis[53]. The physical interaction between mitochondria and LDs observed in this
408 study may very well facilitate both mitochondrial activity and triacylglyceride synthesis, ultimately fueling the
409 survival of residual cells. Further studies will be necessary to test this using an in vitro system that can be
410 manipulated and imaged with proteins of interest tagged, which, unfortunately, is currently infeasible in PDX
411 models. Nonetheless, mapping the connections between mitochondria and key organelles promises to provide
412 critical insights into essential subcellular mechanisms of communication[7,21,69,71-74].

413 We found that mitochondrial structural adaptations were more pronounced in tumors treated with a single-
414 agent compared to those with a combination chemotherapies in PIM001-P, but not in WHIM14. Although
415 combining chemotherapies or paring chemotherapies with other drugs can improve treatment efficacy, there is
416 also compelling evidence of drug antagonism or weak additive effects[75-77]. In fact, our recent TNBC PDX study
417 demonstrated that CRB or DTX alone were almost always more efficacious than their combination was, which
418 only provided benefit in 9% of the models tested. Surprisingly, and quite concerningly, 12% of models tested
419 exhibited antagonism between the two chemotherapies[40]. Therefore, it is crucial to continue in depth
420 comparisons of conventional chemotherapy agents administered to TNBC patients every day. Our data indicate
421 that the combining and scheduling of chemotherapies affects the ability of mitochondria to adapt, an insight that
422 may be critical for the future success of mitochondria-targeting therapies developed for TNBC patients[78].

423 We also observed extensive mITH, particularly in the TN tumors. Mitochondrial structural heterogeneity is
424 tissue-specific and reflects the mitochondrial demands of the tissue. For example, skeletal muscle, which
425 contains a mixture of mitochondria-rich and mitochondria-poor fibers, exhibits greater mitochondrial structural
426 heterogeneity than cardiac muscle, which requires continuous ATP due to continuous contraction[27]. Similarly,
427 mitochondria in neuronal axons and dendrites adopt different morphologies that match the differing energy
428 demands of these neuronal compartments[30]. Thus, the mitochondrial ITH observed in TN tumors may parallel

429 the spatial heterogeneity of proteins and other molecules reported in human TNBC specimens[57,79,80].
430 Heterogeneous mitochondria may provide energetic adaptability that supports cell survival under stressors, such
431 as chemotherapy, although this remains to be experimentally tested. All chemotherapy treatments we examined
432 markedly reduced mitochondrial ITH, suggesting that mitochondria may undergo a 'bottleneck' to sustain cell
433 survival following chemotherapeutic assault. Previous studies in breast cancer have shown enrichment of a
434 cancer stem cell-like, or 'tumor-initiating cell,' subpopulation after a variety of therapeutic exposures[81,82]. Another
435 potential mechanism underpinning these changes is the dynamic adaptation of mitochondrial structure in
436 response to chemotherapy, which may arise broadly across cells rather than being restricted to a subpopulation
437 or clone. Substantial evidence supports this mechanism[8,13,83,84] Indeed, mitochondria are highly dynamic
438 organelles, with fusion and fission coordinated with multiple cellular processes including the cell cycle[7,21].

439 Mitochondria are not static organelles; rather, cycles of fission and fusion support their dynamic nature[21,62,71].
440 Our imaging captured only a snapshot of mitochondrial structures in our tumor samples, which we suspect
441 represents the 'average' mitochondrial state in each tumor specimen. As 3D methods with subcellular resolution
442 advance to enable longitudinal or even real-time analyses, it may become possible to evaluate the rates of
443 mitochondrial structural changes in experimental models[18,29,68,74,85-87]. As we showed previously, both
444 pharmacologic and genetic perturbations can induce these mitochondrial structures[11]. It is reasonable to
445 speculate that these structures are plastic and reversible, as reported prior in this PDX model, PIM001-P, treated
446 with AC, where a reversible drug-tolerant state was observed[13].

---

447 Our study has several limitations. While SBF-SEM provides detailed information on the 3D landscape of
448 subcellular organelles[18], it is exceptionally labor- and time-intensive, requiring specialized expertise[18], which
449 limits its routine use in research labs and in the clinic. For this reason, we performed an in-depth analysis of
450 mitochondria for one tumor per treatment group, selecting spatially distinct ROIs for mitochondrial quantification
451 to account for possible spatial heterogeneity within each tumor. It remains to be determined how reproducible
452 mitochondrial features will be across large cohorts of human tumors. However, based on the similarities between
453 the two single-agent groups as well as between the two combination groups, we suspect that our findings may
454 be generalizable to a sizable subset of TNBC patients. Although efforts are underway to use AI or automate
455 mitochondria and other organelle analyses, algorithms often need to be retrained on new data sets[88]. It is also

critically important to expand these studies to additional TNBC specimens from other patients because inter-patient heterogeneity within TNBC is well documented at the DNA, RNA, and protein levels[48,80,89]. Increasing interest in including 3D modeling underscores its potential to provide a more comprehensive understanding of cancer progression and drug responses from morphological perspective[90,91]. Mitochondrial structural differences among TNBC subtypes have not yet been characterized but will be important in future research. Finally, PDX models lack a fully intact immune system and are highly sensitive to chemotherapy toxicities; thus, it will be essential to validate these findings in human tumor specimens with a fully intact microenvironment. Nonetheless, work from our group and many others have shown PDX models faithfully capture key features of human cancer, including ITH, metabolic phenotypes, and chemotherapeutic responses[33,92,93].

REFERENCES CITED

1 Harbeck, N. *et al.* Breast cancer. *Nat Rev Dis Primers* **5**, 66 (2019). https://doi.org:10.1038/s41572-019-0111-2

2 Bianchini, G., De Angelis, C., Licata, L. & Gianni, L. Treatment landscape of triple-negative breast cancer - expanded options, evolving needs. *Nat Rev Clin Oncol* **19**, 91-113 (2022). https://doi.org:10.1038/s41571-021-00565-2

3 Schmid, P. *et al.* Pembrolizumab for Early Triple-Negative Breast Cancer. *N Engl J Med* **382**, 810-821 (2020). https://doi.org:10.1056/NEJMoa1910549

4 Vagia, E., Mahalingam, D. & Cristofanilli, M. The Landscape of Targeted Therapies in TNBC. *Cancers (Basel)* **12** (2020). https://doi.org:10.3390/cancers12040916

5 Symmans, W. F. *et al.* Long-Term Prognostic Risk After Neoadjuvant Chemotherapy Associated With Residual Cancer Burden and Breast Cancer Subtype. *J Clin Oncol* **35**, 1049-1060 (2017). https://doi.org:10.1200/JCO.2015.63.1010

6 Yau, C. *et al.* Residual cancer burden after neoadjuvant chemotherapy and long-term survival outcomes in breast cancer: a multicentre pooled analysis of 5161 patients. *Lancet Oncol* **23**, 149-160 (2022). https://doi.org:10.1016/S1470-2045(21)00589-1

7 Jenkins, B. C. *et al.* Mitochondria in disease: changes in shapes and dynamics. *Trends Biochem Sci* **49**, 346-360 (2024). https://doi.org:10.1016/j.tibs.2024.01.011

8 Pendleton, K. E., Wang, K. & Echeverria, G. V. Rewiring of mitochondrial metabolism in therapy-resistant cancers: permanent and plastic adaptations. *Front Cell Dev Biol* **11**, 1254313 (2023). https://doi.org:10.3389/fcell.2023.1254313

9 Zhao, J. *et al.* Mitochondrial dynamics regulates migration and invasion of breast cancer cells. *Oncogene* **32**, 4814-4824 (2013). https://doi.org:10.1038/onc.2012.494

10 Humphries, B. A. *et al.* Enhanced mitochondrial fission suppresses signaling and metastasis in triple-negative breast cancer. *Breast Cancer Res* **22**, 60 (2020). https://doi.org:10.1186/s13058-020-01301-x

11 Baek, M. L. *et al.* Mitochondrial structure and function adaptation in residual triple negative breast cancer cells surviving chemotherapy treatment. *Oncogene* **42**, 1117-1131 (2023). https://doi.org:10.1038/s41388-023-02596-8

12 Herkenne, S. *et al.* Developmental and Tumor Angiogenesis Requires the Mitochondria-Shaping Protein Opa1. *Cell Metab* **31**, 987-1003 e1008 (2020). https://doi.org:10.1016/j.cmet.2020.04.007

13 Echeverria, G. V. *et al.* Resistance to neoadjuvant chemotherapy in triple-negative breast cancer mediated by a reversible drug-tolerant state. *Sci Transl Med* **11** (2019). https://doi.org:10.1126/scitranslmed.aav0936

14 Herkenne, S. *et al.* Developmental and Tumor Angiogenesis Requires the Mitochondria-Shaping Protein Opa1. *Cell Metab* **31**, 987-1003.e1008 (2020). https://doi.org:10.1016/j.cmet.2020.04.007
15 Pellattiero, A. *et al.* Small molecule OPA1 inhibitors amplify cytochrome c release and reverse cancer cells resistance to Bcl-2 inhibitors. *Sci Adv* **11**, eadx4562 (2025). https://doi.org:10.1126/sciadv.adx4562
16 Denk, W. & Horstmann, H. Serial block-face scanning electron microscopy to reconstruct three-dimensional tissue nanostructure. *PLoS Biol* **2**, e329 (2004). https://doi.org:10.1371/journal.pbio.0020329
17 Jiao, W., Chatton, J. Y. & Genoud, C. Mitochondria morphometry in 3D datasets obtained from mouse brains with serial block-face scanning electron microscopy. *Methods Cell Biol* **177**, 197-211 (2023). https://doi.org:10.1016/bs.mcb.2023.01.021
18 Marshall, A. G. *et al.* Serial Block Face-Scanning Electron Microscopy as a Burgeoning Technology. *Adv Biol (Weinh)* **7**, e2300139 (2023). https://doi.org:10.1002/adbi.202300139
19 Garza-Lopez, E. *et al.* Correction: Garza-Lopez et al. Protocols for Generating Surfaces and Measuring 3D Organelle Morphology Using Amira. Cells 2022, 11, 65. *Cells* **12** (2023). https://doi.org:10.3390/cells12101356
20 Garza-Lopez, E. *et al.* Protocols for Generating Surfaces and Measuring 3D Organelle Morphology Using Amira. *Cells* **11** (2021). https://doi.org:10.3390/cells11010065
21 Glancy, B., Kim, Y., Katti, P. & Willingham, T. B. The Functional Impact of Mitochondrial Structure Across Subcellular Scales. *Front Physiol* **11**, 541040 (2020). https://doi.org:10.3389/fphys.2020.541040
22 Beasley, H. K., Rodman, T. A., Collins, G. V., Hinton, A., Jr. & Exil, V. TMEM135 is a Novel Regulator of Mitochondrial Dynamics and Physiology with Implications for Human Health Conditions. *Cells* **10** (2021). https://doi.org:10.3390/cells10071750
23 Hinton, A., Jr. *et al.* A Comprehensive Approach to Sample Preparation for Electron Microscopy and the Assessment of Mitochondrial Morphology in Tissue and Cultured Cells. *Adv Biol (Weinh)* **7**, e2200202 (2023). https://doi.org:10.1002/adbi.202200202
24 Neikirk, K. *et al.* Systematic Transmission Electron Microscopy-Based Identification and 3D Reconstruction of Cellular Degradation Machinery. *Adv Biol (Weinh)* **7**, e2200221 (2023). https://doi.org:10.1002/adbi.202200221
25 Chen, L. *et al.* Positive feedback loop between mitochondrial fission and Notch signaling promotes survivin-mediated survival of TNBC cells. *Cell Death Dis* **9**, 1050 (2018). https://doi.org:10.1038/s41419-018-1083-y
26 Si, L. *et al.* Silibinin inhibits migration and invasion of breast cancer MDA-MB-231 cells through induction of mitochondrial fusion. *Mol Cell Biochem* **463**, 189-201 (2020). https://doi.org:10.1007/s11010-019-03640-6
27 Vincent, A. E. *et al.* Quantitative 3D Mapping of the Human Skeletal Muscle Mitochondrial Network. *Cell Rep* **26**, 996-1009 e1004 (2019). https://doi.org:10.1016/j.celrep.2019.01.010
28 Vue, Z. *et al.* Three-dimensional mitochondria reconstructions of murine cardiac muscle changes in size across aging. *Am J Physiol Heart Circ Physiol* **325**, H965-H982 (2023). https://doi.org:10.1152/ajpheart.00202.2023
29 Vue, Z. *et al.* 3D reconstruction of murine mitochondria reveals changes in structure during aging linked to the MICOS complex. *Aging Cell* **22**, e14009 (2023). https://doi.org:10.1111/acel.14009
30 Faitg, J. *et al.* 3D neuronal mitochondrial morphology in axons, dendrites, and somata of the aging mouse hippocampus. *Cell Rep* **36**, 109509 (2021). https://doi.org:10.1016/j.celrep.2021.109509
31 Jadav, N. *et al.* Beyond the surface: Investigation of tumorsphere morphology using volume electron microscopy. *J Struct Biol* **215**, 108035 (2023). https://doi.org:10.1016/j.jsb.2023.108035
32 Han, M. *et al.* Spatial mapping of mitochondrial networks and bioenergetics in lung cancer. *Nature* **615**, 712-719 (2023). https://doi.org:10.1038/s41586-023-05793-3
33 Bruna, A. *et al.* A Biobank of Breast Cancer Explants with Preserved Intra-tumor Heterogeneity to Screen Anticancer Compounds. *Cell* **167**, 260-274 e222 (2016). https://doi.org:10.1016/j.cell.2016.08.041
34 Dobrolecki, L. E. *et al.* Patient-derived xenograft (PDX) models in basic and translational breast cancer research. *Cancer Metastasis Rev* **35**, 547-573 (2016). https://doi.org:10.1007/s10555-016-9653-x

35 Echeverria, G. V. *et al.* High-resolution clonal mapping of multi-organ metastasis in triple negative breast cancer. *Nat Commun* **9**, 5079 (2018). https://doi.org:10.1038/s41467-018-07406-4

36 Eirew, P. *et al.* Dynamics of genomic clones in breast cancer patient xenografts at single-cell resolution. *Nature* **518**, 422-426 (2015). https://doi.org:10.1038/nature13952

37 Savage, P. *et al.* Chemogenomic profiling of breast cancer patient-derived xenografts reveals targetable vulnerabilities for difficult-to-treat tumors. *Commun Biol* **3**, 310 (2020). https://doi.org:10.1038/s42003-020-1042-x

38 Baek, M., Chang, J. T. & Echeverria, G. V. Methodological Advancements for Investigating Intra-tumoral Heterogeneity in Breast Cancer at the Bench and Bedside. *J Mammary Gland Biol Neoplasia* **25**, 289-304 (2020). https://doi.org:10.1007/s10911-020-09470-3

39 Eccles, S. A. *et al.* Critical research gaps and translational priorities for the successful prevention and treatment of breast cancer. *Breast Cancer Res* **15**, R92 (2013). https://doi.org:10.1186/bcr3493

40 Lei, J. T. *et al.* Patient-Derived Xenografts of Triple-Negative Breast Cancer Enable Deconvolution and Prediction of Chemotherapy Responses. *bioRxiv* (2025). https://doi.org:10.1101/2024.12.09.627518

41 Anurag, M. *et al.* Proteogenomic Markers of Chemotherapy Resistance and Response in Triple-Negative Breast Cancer. *Cancer Discov* **12**, 2586-2605 (2022). https://doi.org:10.1158/2159-8290.CD-22-0200

42 Virtanen, P. *et al.* SciPy 1.0: fundamental algorithms for scientific computing in Python. *Nat Methods* **17**, 261-272 (2020). https://doi.org:10.1038/s41592-019-0686-2

43 Seabold, S., and Perktold, J. . Statsmodels: Econometric and statistical modeling with python. *Proceedings of the 9th python in science conference* (2010). https://doi.org:10.25080/Majora-92bf1922-011

44 McKinney, W. *Data structures for statistical computing in python*. (2010).

45 Team, R. C. *R: A Language and Environment for Statistical Computing*, <<https://www.R-project.org/>> (2023).

46 Li, S. *et al.* Endocrine-therapy-resistant ESR1 variants revealed by genomic characterization of breast-cancer-derived xenografts. *Cell Rep* **4**, 1116-1130 (2013). https://doi.org:10.1016/j.celrep.2013.08.022

47 Fisher, E. R. *et al.* Pathobiology of preoperative chemotherapy: findings from the National Surgical Adjuvant Breast and Bowel (NSABP) protocol B-18. *Cancer* **95**, 681-695 (2002). https://doi.org:10.1002/cncr.10741

48 Shah, S. P. *et al.* The clonal and mutational evolution spectrum of primary triple-negative breast cancers. *Nature* **486**, 395-399 (2012). https://doi.org:10.1038/nature10933

49 Wang, Y. *et al.* Clonal evolution in breast cancer revealed by single nucleus genome sequencing. *Nature* **512**, 155-160 (2014). https://doi.org:10.1038/nature13600

50 Nik-Zainal, S. *et al.* The life history of 21 breast cancers. *Cell* **149**, 994-1007 (2012). https://doi.org:10.1016/j.cell.2012.04.023

51 Risom, T. *et al.* Differentiation-state plasticity is a targetable resistance mechanism in basal-like breast cancer. *Nat Commun* **9**, 3815 (2018). https://doi.org:10.1038/s41467-018-05729-w

52 Kim, C. *et al.* Chemoresistance Evolution in Triple-Negative Breast Cancer Delineated by Single-Cell Sequencing. *Cell* https://doi.org:10.1016/j.cell.2018.03.041

53 Li, X. *et al.* Intrinsic resistance of tumorigenic breast cancer cells to chemotherapy. *J Natl Cancer Inst* **100**, 672-679 (2008). https://doi.org:10.1093/jnci/djn123

54 Ali, H. R. *et al.* Imaging mass cytometry and multiplatform genomics define the phenogenomic landscape of breast cancer. *Nature Cancer* **1**, 163-175 (2020). https://doi.org:10.1038/s43018-020-0026-6

55 Fischer, J. R. *et al.* Multiplex imaging of breast cancer lymph node metastases identifies prognostic single-cell populations independent of clinical classifiers. *Cell Rep Med* **4**, 100977 (2023). https://doi.org:10.1016/j.xcrm.2023.100977

56 Gruosso, T. *et al.* Spatially distinct tumor immune microenvironments stratify triple-negative breast cancers. *J Clin Invest* **129**, 1785-1800 (2019). https://doi.org:10.1172/JCI96313

57 Wagner, J. *et al.* A Single-Cell Atlas of the Tumor and Immune Ecosystem of Human Breast Cancer. *Cell* **177**, 1330-1345 e1318 (2019). https://doi.org:10.1016/j.cell.2019.03.005

58 Benador, I. Y. *et al.* Mitochondria Bound to Lipid Droplets Have Unique Bioenergetics, Composition, and Dynamics that Support Lipid Droplet Expansion. *Cell Metab* **27**, 869-885 e866 (2018). https://doi.org:10.1016/j.cmet.2018.03.003
59 Benador, I. Y., Veliova, M., Liesa, M. & Shirihai, O. S. Mitochondria Bound to Lipid Droplets: Where Mitochondrial Dynamics Regulate Lipid Storage and Utilization. *Cell Metab* **29**, 827-835 (2019). https://doi.org:10.1016/j.cmet.2019.02.011
60 Cortes, J. *et al.* Pembrolizumab plus chemotherapy versus placebo plus chemotherapy for previously untreated locally recurrent inoperable or metastatic triple-negative breast cancer (KEYNOTE-355): a randomised, placebo-controlled, double-blind, phase 3 clinical trial. *Lancet* **396**, 1817-1828 (2020). https://doi.org:10.1016/S0140-6736(20)32531-9
61 Hinton, A., Jr. *et al.* ATF4-dependent increase in mitochondrial-endoplasmic reticulum tethering following OPA1 deletion in skeletal muscle. *J Cell Physiol* **239**, e31204 (2024). https://doi.org:10.1002/jcp.31204
62 Robertson, G. L. *et al.* DRP1 mutations associated with EMPF1 encephalopathy alter mitochondrial membrane potential and metabolic programs. *J Cell Sci* **136** (2023). https://doi.org:10.1242/jcs.260370
63 Filadi, R. *et al.* TOM70 Sustains Cell Bioenergetics by Promoting IP3R3-Mediated ER to Mitochondria Ca(2+) Transfer. *Curr Biol* **28**, 369-382 e366 (2018). https://doi.org:10.1016/j.cub.2017.12.047
64 Giorgi, C., Marchi, S. & Pinton, P. The machineries, regulation and cellular functions of mitochondrial calcium. *Nat Rev Mol Cell Biol* **19**, 713-730 (2018). https://doi.org:10.1038/s41580-018-0052-8
65 Szymanski, J. *et al.* Interaction of Mitochondria with the Endoplasmic Reticulum and Plasma Membrane in Calcium Homeostasis, Lipid Trafficking and Mitochondrial Structure. *Int J Mol Sci* **18** (2017). https://doi.org:10.3390/ijms18071576
66 Neikirk, K. *et al.* Call to action to properly utilize electron microscopy to measure organelles to monitor disease. *Eur J Cell Biol* **102**, 151365 (2023). https://doi.org:10.1016/j.ejcb.2023.151365
67 Yu, H., Sun, C., Gong, Q. & Feng, D. Mitochondria-Associated Endoplasmic Reticulum Membranes in Breast Cancer. *Front Cell Dev Biol* **9**, 629669 (2021). https://doi.org:10.3389/fcell.2021.629669
68 Crabtree, A. *et al.* Quantitative assessment of morphological changes in lipid droplets and lipid-mito interactions with aging in brown adipose. *J Cell Physiol* **239**, e31340 (2024). https://doi.org:10.1002/jcp.31340
69 Jarc, E. & Petan, T. Lipid Droplets and the Management of Cellular Stress. *Yale J Biol Med* **92**, 435-452 (2019).
70 Viale, A. *et al.* Oncogene ablation-resistant pancreatic cancer cells depend on mitochondrial function. *Nature* **514**, 628-632 (2014). https://doi.org:10.1038/nature13611
71 Katti, P., Ajayi, P. T., Aponte, A., Bleck, C. K. E. & Glancy, B. Identification of evolutionarily conserved regulators of muscle mitochondrial network organization. *Nat Commun* **13**, 6622 (2022). https://doi.org:10.1038/s41467-022-34445-9
72 Glancy, B. & Balaban, R. S. Role of mitochondrial Ca2+ in the regulation of cellular energetics. *Biochemistry* **51**, 2959-2973 (2012). https://doi.org:10.1021/bi2018909
73 Lam, J. *et al.* A Universal Approach to Analyzing Transmission Electron Microscopy with ImageJ. *Cells* **10** (2021). https://doi.org:10.3390/cells10092177
74 Shao, B. *et al.* Ablation of Sam50 is associated with fragmentation and alterations in metabolism in murine and human myotubes. *J Cell Physiol* **239**, e31293 (2024). https://doi.org:10.1002/jcp.31293
75 Osborne, C. K., Kitten, L. & Arteaga, C. L. Antagonism of chemotherapy-induced cytotoxicity for human breast cancer cells by antiestrogens. *J Clin Oncol* **7**, 710-717 (1989). https://doi.org:10.1200/JCO.1989.7.6.710
76 Palmer, A. C., Chidley, C. & Sorger, P. K. A curative combination cancer therapy achieves high fractional cell killing through low cross-resistance and drug additivity. *Elife* **8** (2019). https://doi.org:10.7554/eLife.50036
77 Plana, D., Palmer, A. C. & Sorger, P. K. Independent Drug Action in Combination Therapy: Implications for Precision Oncology. *Cancer Discov* **12**, 606-624 (2022). https://doi.org:10.1158/2159-8290.CD-21-0212
78 Bu, H. *et al.* Spinal IFN-gamma-induced protein-10 (CXCL10) mediates metastatic breast cancer-induced bone pain by activation of microglia in rat models. *Breast Cancer Res Treat* **143**, 255-263 (2014). https://doi.org:10.1007/s10549-013-2807-4

79 Ali, H. R. *et al.* Imaging mass cytometry and multiplatform genomics define the phenogenomic landscape of breast cancer. *Nat Cancer* **1**, 163-175 (2020). https://doi.org:10.1038/s43018-020-0026-6
80 Jackson, H. W. *et al.* The single-cell pathology landscape of breast cancer. *Nature* **578**, 615-620 (2020). https://doi.org:10.1038/s41586-019-1876-x
81 Creighton, C. J. *et al.* Residual breast cancers after conventional therapy display mesenchymal as well as tumor-initiating features. *Proc Natl Acad Sci U S A* **106**, 13820-13825 (2009). https://doi.org:10.1073/pnas.0905718106
82 Balko, J. M. *et al.* Profiling of residual breast cancers after neoadjuvant chemotherapy identifies DUSP4 deficiency as a mechanism of drug resistance. *Nat Med* **18**, 1052-1059 (2012). https://doi.org:10.1038/nm.2795
83 Kim, C. *et al.* Chemoresistance Evolution in Triple-Negative Breast Cancer Delineated by Single-Cell Sequencing. *Cell* **173**, 879-893 e813 (2018). https://doi.org:10.1016/j.cell.2018.03.041
84 Almendro, V. *et al.* Inference of tumor evolution during chemotherapy by computational modeling and in situ analysis of genetic and phenotypic cellular diversity. *Cell Rep* **6**, 514-527 (2014). https://doi.org:10.1016/j.celrep.2013.12.041
85 Crabtree, A. *et al.* Defining Mitochondrial Cristae Morphology Changes Induced by Aging in Brown Adipose Tissue. *Adv Biol (Weinh)* **8**, e2300186 (2024). https://doi.org:10.1002/adbi.202300186
86 Marshall, A. G., Krystofiak, E., Damo, S. M. & Hinton, A., Jr. Correlative light-electron microscopy: integrating dynamics to structure. *Trends Biochem Sci* **48**, 826-827 (2023). https://doi.org:10.1016/j.tibs.2023.05.003
87 Scudese, E. *et al.* 3D Mitochondrial Structure in Aging Human Skeletal Muscle: Insights Into MFN-2-Mediated Changes. *Aging Cell* **24**, e70054 (2025). https://doi.org:10.1111/acel.70054
88 Heinrich, L. *et al.* Whole-cell organelle segmentation in volume electron microscopy. *Nature* **599**, 141-146 (2021). https://doi.org:10.1038/s41586-021-03977-3
89 Lehmann, B. D. *et al.* Identification of human triple-negative breast cancer subtypes and preclinical models for selection of targeted therapies. *J Clin Invest* **121**, 2750-2767 (2011). https://doi.org:10.1172/JCI45014
90 Rozenblatt-Rosen, O. *et al.* The Human Tumor Atlas Network: Charting Tumor Transitions across Space and Time at Single-Cell Resolution. *Cell* **181**, 236-249 (2020). https://doi.org:10.1016/j.cell.2020.03.053
91 Johnson, B. E. *et al.* An omic and multidimensional spatial atlas from serial biopsies of an evolving metastatic breast cancer. *Cell Rep Med* **3**, 100525 (2022). https://doi.org:10.1016/j.xcrm.2022.100525
92 Petrosyan, V. *et al.* Identifying biomarkers of differential chemotherapy response in TNBC patient-derived xenografts with a CTD/WGCNA approach. *iScience* **26**, 105799 (2023). https://doi.org:10.1016/j.isci.2022.105799
93 Guillen, K. P. *et al.* A human breast cancer-derived xenograft and organoid platform for drug discovery and precision oncology. *Nat Cancer* **3**, 232-250 (2022). https://doi.org:10.1038/s43018-022-00337-6

ACKNOWLEDGEMENTS

We thank the breast cancer patients who donated their biopsies for PDX models. The generation of the PDX model PIM001-P was supported by a generous gift from the Cazalot family and the MD Anderson Women's Cancer Moonshot Program. Dr. Helen Piwnica-Worms provided the PIM001-P PDX model via a materials transfer agreement. The BCM Patient Derived Xenograft Core guided the treatment regimens for DTX, CRB, DTX+CRB funded by CPRIT Core Facility Award (RP220646) and P30 Cancer Center Support Grant (NCI-CA125123). Dr. Junegoo Lee and Ms. Emily Goff aided with animal experiments. Dr. Tao Wang provided guidance for statistical analyses. Ms. Janice Cowden provided patient research advocacy support. The Mayo

704 Clinic Microscopy and Cell Analysis Core provided experimental technical support. H&E, Ku80, and human
705 mitochondria staining of PDX tumor sections were conducted at the BCM Pathology Core and Lab, supported
706 by the Breast Center and a variety of research grants awarded to its faculty, including one of nine Specialized
707 Programs of Research Excellence (SPORE) in Breast Cancer granted by the National Institute of Health. S10
708 grant (1S10OD028671-01) for digital imaging of the IHC slides. Dr. George Miles aided with the histological
709 review of IHC and H&E-stained slides.

710

711 **DATA AND CODE AVAILABILITY**

712 Mitochondria images and raw data are available from the corresponding authors upon request. All computational
713 codes used for statistical analyses are available https://github.com/audra-lane/berner-et-al-2024. The PDX
714 model PIM001-P can be made available through a materials transfer agreement with The University of Texas
715 MD Anderson Cancer Center. The PDX model WHIM14 can be made available through a materials transfer
716 agreement with Dr. Shunquan Li (shunqiangli@wustl.edu)

717

718 **FUNDING**

719 GVE is a CPRIT Scholar in Cancer Research. Funding sources that supported this work include the Cancer
720 Prevention and Research Institute of Texas RR200009 (to GVE); NIH 1K22CA241113-01 (to GVE); NIH T32
721 predoctoral training grant T32GM136560-02 (to MJB); BWF Ad-hoc Award, National Institutes of Health (NIH)
722 Small Research Pilot Subaward to 5R25HL106365-12 from the NIH PRIDE Program, DK020593 (to AHJ);
723 1R37CA269783-01A1 (to GVE); a BCM Breast Program SPORE Career Enhancement Program Grant (to GVE);
724 National Science Foundation Graduate Research Fellowship 2140736 (to MJB); American Cancer Society
725 Research Scholar Grant RSG-22-093-01-CCB (to GVE), a Myra Branum Wilson Baylor Research Advocates for
726 Student Scientists Scholarship (to MJB); and a Breast Cancer Alliance Young Investigator Grant (to GVE);
727 UNCF/Bristol-Myers Squibb (UNCF/BMS) E.E. Just Postgraduate Fellowship in Life Sciences Fellowship and
728 Burroughs Wellcome Fund/ PDEP #1022376 (to HKB) UNCF/BMS E.E. Just Faculty Fund, Career Award at the
729 Scientific Interface (CASI Award) from Burroughs Welcome Fund ID # 1021868.01, Vanderbilt Diabetes and
730 Research Training Center for Department of Medicine's Diabetes Research and Training Center (DRTC)

731 Alzheimer's Disease Pilot & Feasibility Program, CZI Science Diversity Leadership grant number 2022-
732 253529 from the Chan Zuckerberg Initiative DAF, and an advised fund of Silicon Valley Community Foundation
733 (to AHJ). The content is solely the responsibility of the authors and does not necessarily represent the official
734 views of the National Institutes of Health, the Cancer Prevention and Research Institute of Texas, National
735 Science Foundation, American Cancer Society, BRASS, UNCF/BMS, Burroughs Welcome Fund, DRTC, Chan
736 Zuckerberg Initiative DAF, or Silicon Valley Community Foundation.
737

738 **AUTHOR CONTRIBUTIONS**

739 MJB, HKB, AOH, and GVE were responsible for the overall study design, experimentation, data interpretation,
740 and writing of the manuscript.
741 AL conducted statistical analyses under the supervision of GVE.
742 SWW aided in PDX model treatment studies under the supervision of GVE.
743 BR, ZV, BS, FZ, MK, LV, AGM, AP, AK, CV, PV, PK, AC, DP, JSR, and ES aided in mitochondrial
744 segmentation, analysis, and 3D rendering of figures and videos under the supervision of AOH.
745 MLB aided in PDX model treatment study design, implementation, and mitochondrial imaging under the
746 supervision of GVE.
747 LED aided in the chemotherapeutic regimen design and dosing of PDX mice under the supervision of MTL.
748

749 **FIGURE LEGENDS**

750 **Figure 1. PIM001-P PDX tumors persisted following conventional chemotherapy treatments.** (a)
751 Schematic of the experimental approach used in the study. Images were adapted from BioRender. (b) Tumor
752 volumes were monitored biweekly following administration of chemotherapies to mice bearing orthotopic
753 PIM001-P tumors (n = 6 mice/group). Treatment groups were treatment-naïve (TN), Adriamycin +
754 cyclophosphamide (AC), docetaxel + carboplatin (DTX+CRB), docetaxel (DTX), and carboplatin (CRB). Arrows
755 at the top indicate when chemotherapy was administered. Asterisks (*) above the x-axis indicate early euthanasia
756 due to animal health concerns. Residual tumors were harvested, as noted by arrows. Error bars represent the

757 standard error of the mean. (c) Residual tumors were harvested, processed for FFPE, and analyzed by H&E
758 staining and IHC for Ki67, Ku80 and human-specific mitochondria. Scale bars are 50 μm.
759
760 **Figure 2. Single-agent chemotherapy treatments in PIM001-P significantly increased mitochondrial size**
761 **in residual tumors relative to TN**. (a-e) Representative SBF-SM orthoslices. (a'-e') Representative 3D SBF-
762 SEM orthoslices with overlays of mitochondria segmentations. (a''-e'') Representative 3D SBF-SEM
763 mitochondria segmentations for each treatment group: treatment-naïve (TN), Adriamycin + cyclophosphamide
764 (AC), docetaxel + carboplatin (DTX+CRB), docetaxel (DTX), and carboplatin (CRB). The scale bar is 3 μm.
765 Mitochondrial measurements were calculated using Amira software for 350 segmented mitochondria
766 (represented as dots) from each tumor for (f) 3D volume, (g) 3D area, (h), and perimeter. Adjusted p-values (*p
767 < 0.05, **p < 0.01, ***p < 0.001, ****p<0.0001) are shown on box and whisker plots as determined using the
768 Mann–Whitney U test followed by the Holm method.
769
770 **Figure 3. Single-agent chemotherapy treated residual tumors' mitochondria are more branched and less**
771 **spherical relative to TN in PIM001-P.** Mitochondrial networks revealed through 3D mitochondria rendered using
772 SBF-SEM. (a) Representative longitudinal and transverse views of the segmented mitochondria for each
773 treatment group: treatment-naïve (TN), Adriamycin + cyclophosphamide (AC), docetaxel + carboplatin
774 (DTX+CRB), docetaxel (DTX), and carboplatin (CRB). The scale bar is 3 μm. Mitochondrial measurements were
775 calculated using Amira software for 350 segmented mitochondria (represented as dots) from each tumor for (b)
776 sphericity (c) mitochondrial complex index (MCI), along with their respective method of measurements below.
777 Adjusted p-values (*p < 0.05, **p < 0.01, ***p < 0.001, ****p<0.0001) are shown on box and whisker plots as
778 determined using the Mann–Whitney U test followed by the Holm method.
779
780 **Figure 4. PIM001-P mito-otyping of the diverse mitochondrial structures within each treatment group.** (a)
781 Representative mitochondria structures from the bottom, middle, and top 10% of the 3D volume for tumors are
782 displayed. Scale bars are 1μm.
783

784 **Figure 5. The frequency of MLCs increases upon chemotherapy, while the sizes of the contacts decrease**
785 **in WHIM14.** Quantification of how chemotherapy remodels mitochondrial-lipid droplet contacts (MLCs) for each
786 treatment group: treatment-naïve (TN), Adriamycin + cyclophosphamide (AC), docetaxel + carboplatin
787 (DTX+CRB), docetaxel (DTX), and carboplatin (CRB). (a-d'') 3D rendering of the mitochondria in purple, lipid
788 droplets in yellow, and their interaction in red. The scale bar is 2μm. The 3D renders show that TN exhibits
789 relatively few but broad, sheet-like interfaces, whereas all treatment groups display numerous, smaller, punctate
790 contacts scattered across organelles. Consistent with this visual shift, bar plots demonstrate that the fraction of
791 MLCs among the total number of segmented mitochondria (E; % MLC per 500 mitochondria) is higher after
792 treatment than in the TN group. In contrast, per-contact surface area (F) and volume (G) are largest in TN and
793 significantly reduced in all treated conditions, indicating that individual interfaces between the mitochondria and
794 LDs shrink following chemotherapy. This is also displayed in the bar plots, showing the total sum of either surface
795 area (H) or volume of the MLC versus the total sum of each metric for the segmented mitochondria.
796
797 **Supplemental Materials:**
798 **Supplementary Table 1. PIM001-P selected segmented mitochondria used for analyses.** The number of
799 segmented mitochondria characterized during this study and the process for selecting 350 mitochondria per
800 treatment for analysis.
801
802 **Supplementary Table 2. WHIM14 selected segmented mitochondria used for analyses.** The number of
803 segmented mitochondria characterized during this study of the second PDX model, WHIM14. Two ROIs from
804 one residual tumor of each treatment arm were segmented for a minimum of 250 mitochondria each. Random
805 number generator was used to select 500 segmented for each treatment arm to be used in the analysis.
806
807 **Supplementary Table 3. WHIM14 selected segmented lipid droplets used for analyses.** Number of
808 segmented lipid droplets characterized during this study of the second PDX model, WHIM14 for the lipid-
809 mitochondrial interaction analyses. Two ROIs from one residual tumor of each treatment arm were segmented

810 for a minimum of 100 mitochondria each. Random number generator was used to select 200 segmented for
811 each treatment arm to be used in the analysis.
812
813 **Supplementary Figure 1. PDX TNBC tumors persist following conventional chemotherapy treatments in**
814 **WHIM14.**
815 (a) Tumor volumes were monitored biweekly following administration of chemotherapies to mice bearing
816 orthotopic WHIM14 tumors (n = 6 mice/group). Arrows at the top indicate when chemotherapy was administered.
817 Asterisks (*) above the x-axis indicate early euthanasia due to animal health concerns. Residual tumors were
818 harvested, as noted by arrows. Error bars represent the standard error of the mean. (B) Residual tumors were
819 harvested, processed for FFPE, and analyzed by H&E staining, IHC for Ku80, and human-specific mitochondria.
820 Scale bars are 50 μm.
821
822 **Supplementary Figure 2. PIM001-P PDX tumors treated with one cycle of DTX+CRB avoid toxicity and**
823 **persist.** (a) Normalized tumor volume from the day of starting treatment of PIM001-P treated with one dose of
824 DTX+CRB and monitored biweekly (n = 2 TN; n=4 DTX+CRB). Treatment groups were treatment-naïve (TN)
825 and docetaxel + carboplatin (DTX+CRB).
826
827 **Supplementary Figure 3. Several mitochondrial features are significantly increased after single-agent**
828 **chemotherapy treatments in WHIM14.** (a-d) Representative SBF-SEM orthoslices. (a'-d') Representative 3D
829 SBF-SEM orthoslices with overlays of mitochondria segmentations. (a''-d'') Representative 3D SBF-SEM
830 mitochondria segmentations for each treatment group: treatment-naïve (TN), docetaxel + carboplatin
831 (DTX+CRB), docetaxel (DTX), and carboplatin (CRB). The scale bar is 1 μm. Mitochondrial measurements were
832 calculated using Amira software for 500 segmented mitochondria (represented as dots) from each tumor for (e)
833 volume, (f) 3D area, and (g) perimeter. Adjusted p-values (*$p < 0.05$, **$p < 0.01$, ***$p < 0.001$, ****$p<0.0001$) are
834 shown on box and whisker plots as determined using the Mann–Whitney U test followed by the Holm method.
835

836 **Supplementary Figure 4. PIM001-P mitochondrial measurements across treatment groups do not have**
837 **normal distributions.** (a) Q–q plots of the raw measurements across all tumors are shown. Each blue dot
838 represents one of the segmented mitochondria from a total of 350 segmented mitochondria. The red line
839 indicates a reference for where the normal distribution falls on the graph.
840
841 **Supplementary Figure 5. PIM001-P distribution of mitochondrial metrics within each treatment group.**
842 Density plots are of log10 transformed data showing the distribution of the respective metric for the segmented
843 mitochondria. The line indicates the median for treatment-naïve tumors. Treatment groups: treatment-naïve (TN),
844 Adriamycin + cyclophosphamide (AC), docetaxel + carboplatin (DTX+CRB), docetaxel (DTX), and carboplatin
845 (CRB).
846
847 **Supplementary Figure 6. PIM001-P single chemotherapeutic agent treated mitochondria are greater in**
848 **width and length.** Mitochondrial measurements for width and length were calculated using Amira software for
849 350 segmented mitochondria (represented as dots) from each treatment group. Treatment groups: treatment-
850 naïve (TN), Adriamycin + cyclophosphamide (AC), docetaxel + carboplatin (DTX+CRB), docetaxel (DTX), and
851 carboplatin (CRB). (a) Width (b) Length. Adjusted p-values (*$p < 0.05$, **$p < 0.01$, ***$p < 0.001$, ****$p<0.0001$)
852 are shown on box and whisker plots as determined using the Mann–Whitney U test followed by the Holm method.
853 Density plots are of log10 transformed data showing the distribution of the respective metric for the segmented
854 mitochondria. The line indicates the median for treatment-naïve tumors. (c) Density plot for width (d) Density plot
855 for length.
856
857 **Supplementary Figure 7. WHIM14 distribution of mitochondrial metrics within each treatment group.**
858 Density plots are of log10 transformed data showing the distribution of the respective metric for the segmented
859 mitochondria. The line indicates the median for treatment-naïve tumors. Treatment groups: treatment-naïve (TN),
860 docetaxel + carboplatin (DTX+CRB), docetaxel (DTX), and carboplatin (CRB).
861

862 **Supplementary Figure 8. Chemotherapy treatment increased the width and length of mitochondria in**
863 **WHIM14.** Mitochondrial measurements for width and length were calculated using Amira software for 350
864 segmented mitochondria (represented as dots) from each treatment group. Treatment groups: treatment-naïve
865 (TN), docetaxel + carboplatin (DTX+CRB), docetaxel (DTX), and carboplatin (CRB). (a) Width (b) Length.
866 Adjusted p-values (*p < 0.05, **p < 0.01, ***p < 0.001, ****p<0.0001) are shown on box and whisker plots as
867 determined using the Mann–Whitney U test followed by the Holm method. Density plots are of log10 transformed
868 data showing the distribution of the respective metric for the segmented mitochondria. The line indicates the
869 median for treatment-naïve tumors. (c) Density plot for width (d) Density plot for length. Treatment groups:
870 treatment-naïve (TN), docetaxel + carboplatin (DTX+CRB), docetaxel (DTX), and carboplatin (CRB).
871
872 **Supplementary Figure 9. mITH was significantly reduced upon chemotherapy for several mitochondrial**
873 **metrics in PIM001-P.** (a) Schematic for comparing the variance between treatment groups across all
874 mitochondrial features. Treatment groups: treatment-naïve (TN), Adriamycin + cyclophosphamide (AC),
875 docetaxel + carboplatin (DTX+CRB), docetaxel (DTX), and carboplatin (CRB). (b-i) Variance bar graphs for all
876 350 segmented mitochondrial volume, area, perimeter, width, length, mitochondrial branching index (MBI),
877 sphericity, and mitochondrial complex index (MCI). F-test and Holm method for adjusted p-values (*p < 0.05, **p
878 < 0.01, ***p < 0.001, ****p<0.0001).
879
880 **Supplementary Figure 10. WHIM14 treated with DTX+CRB or CRB only had a significant reduction in**
881 **mITH.** Treatment groups: treatment-naïve (TN), docetaxel + carboplatin (DTX+CRB), docetaxel (DTX), and
882 carboplatin (CRB). (a-h) Variance bar graphs for all 500 segmented mitochondrial volume, area, perimeter, width,
883 length, mitochondrial branching index (MBI), sphericity, and mitochondrial complex index (MCI). F-test and Holm
884 method for adjusted p-values (*p < 0.05, **p < 0.01, ***p < 0.001, ****p<0.0001).
885
886 **Supplementary Figure 11. WHIM14 residual tumors' mitochondria are less branched and more spherical**
887 **compared to TN tumors.** Mitochondrial networks revealed through 3D mitochondria rendered using SBF-SEM.
888 (a) Representative longitudinal and transverse views of the segmented mitochondria for each treatment group:

889 treatment-naïve (TN), docetaxel + carboplatin (DTX+CRB), docetaxel (DTX), and carboplatin (CRB). The scale
890 bar is 1 μm. Mitochondrial measurements were calculated using Amira software for 500 segmented mitochondria
891 (represented as dots) from each tumor for (b) sphericity (c) mitochondrial complex index (MCI), along with their
892 respective method of measurements below. Adjusted p-values (*p < 0.05, **p < 0.01, ***p < 0.001, ****p<0.0001)
893 are shown on box and whisker plots as determined using the Mann–Whitney U test followed by the Holm method.
894

895 **Supplementary Figure 12. MBI of PIM001-P and WHIM14.** Mitochondrial branching index (MBI). (a) diagram
896 of MBI calculation. MBI of the segmented mitochondria for each treatment group: treatment-naïve (TN),
897 Adriamycin + cyclophosphamide (AC), docetaxel + carboplatin (DTX+CRB), docetaxel (DTX), and carboplatin
898 (CRB) for the two PDX models in the study. (b) PIM001-PI (c) WHIM14 Adjusted p-values (*p < 0.05, **p < 0.01,
899 ***p < 0.001, ****p<0.0001) are shown on box and whisker plots as determined using the Mann–Whitney U test
900 followed by the Holm method.
901

902 **Supplementary Figure 13. WHIM14 mito-otyping of the diverse mitochondrial structures observed within**
903 **each treatment group.** (a) Representative mitochondria structures from the bottom, middle, and top 10% of the
904 3D volume for tumors are displayed. Scale bars are 0.2μm.
905

906 **Supplementary Figure 14. WHIM14 lipid droplet sizes increase after single-agent chemotherapy**
907 **treatment.** Lipid droplet segmentation of WHIM14 PDX models from each treatment group: treatment-naïve
908 (TN), docetaxel + carboplatin (DTX+CRB), docetaxel (DTX), and carboplatin (CRB). Lipid droplet measurements
909 were calculated using Amira software for 200 segmented lipid droplets (represented as dots) from each tumor
910 for (a) volume, (b) 3D area, and (c) perimeter (d) sphericity (e) lipid droplet complexity index. Adjusted p-values
911 (*p < 0.05, **p < 0.01, ***p < 0.001, ****p<0.0001) are shown on box and whisker plots as determined using the
912 Mann–Whitney U test followed by the Holm method.
913

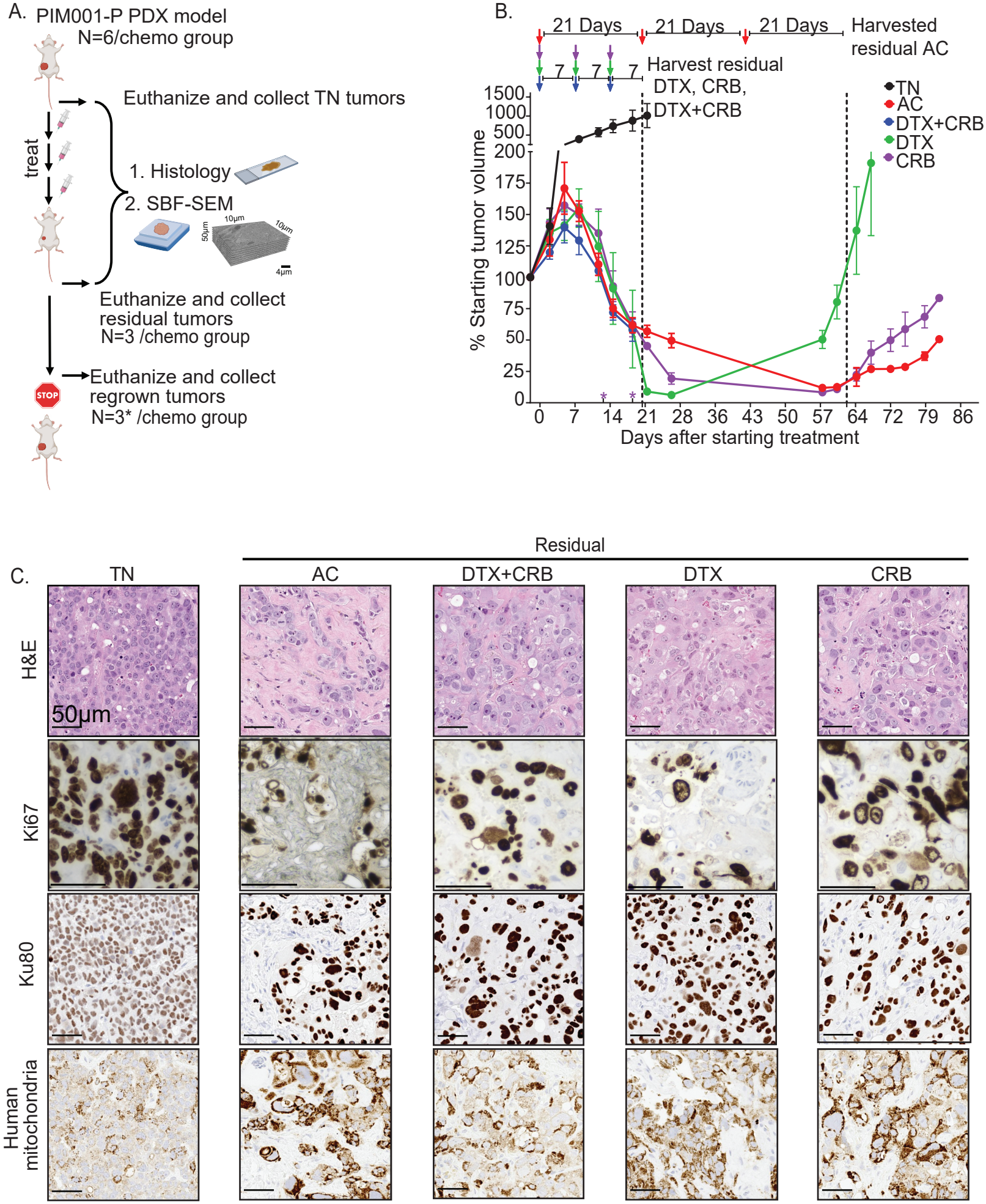

Figure 1. PIM001-P PDX tumors persisted following conventional chemotherapy treatments.

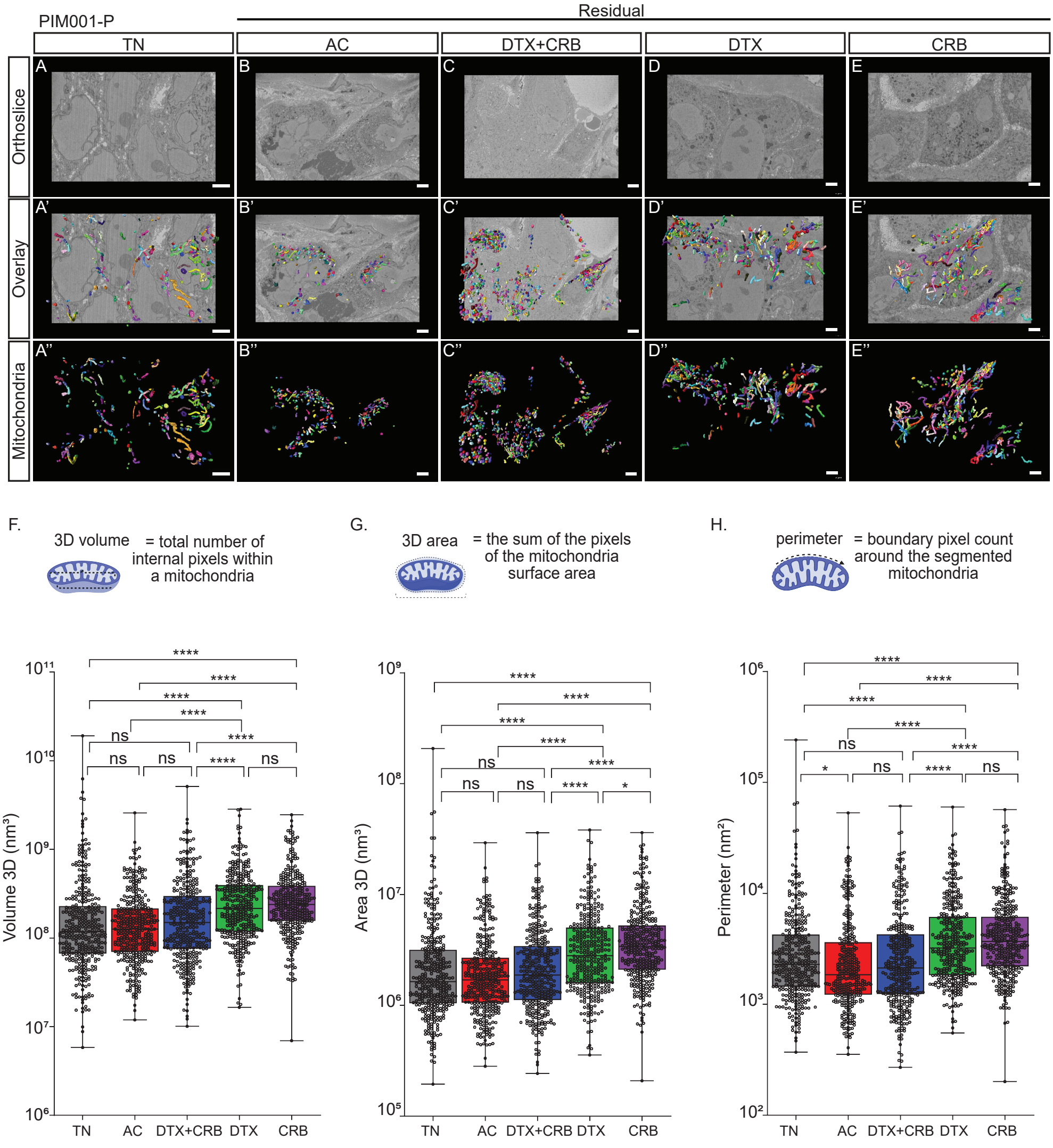

Figure 2. Single-agent chemotherapy treatments in the PIM001-P significantly increased mitochondrial size in residual tumors relative to TN.

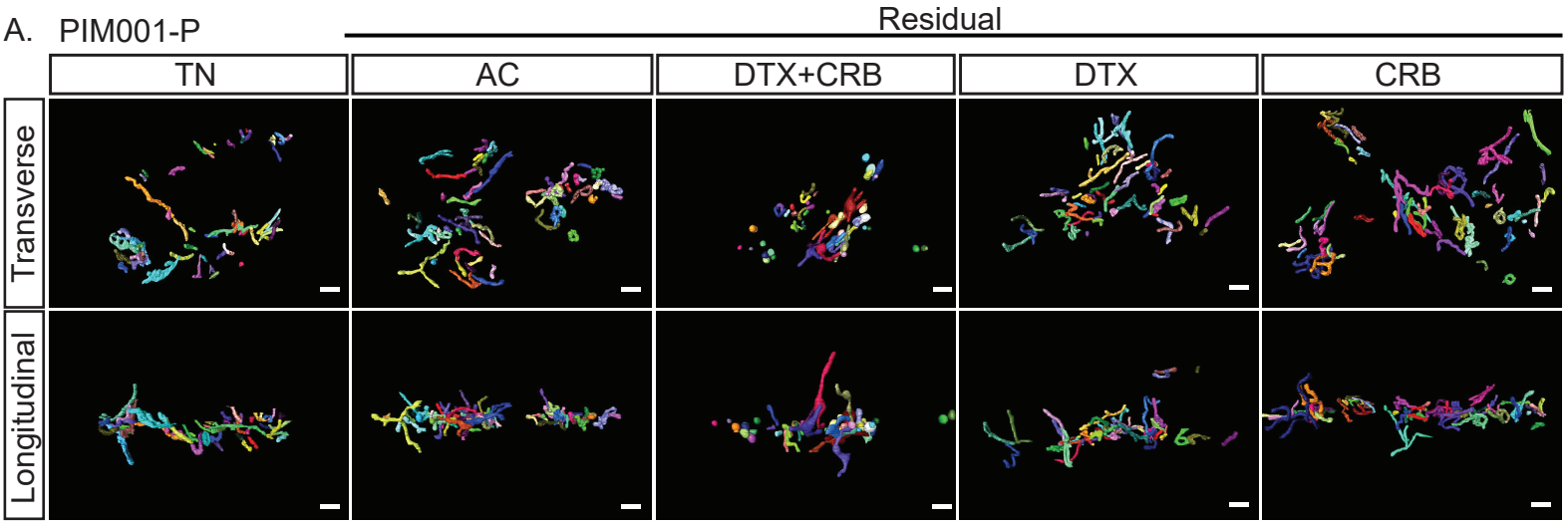

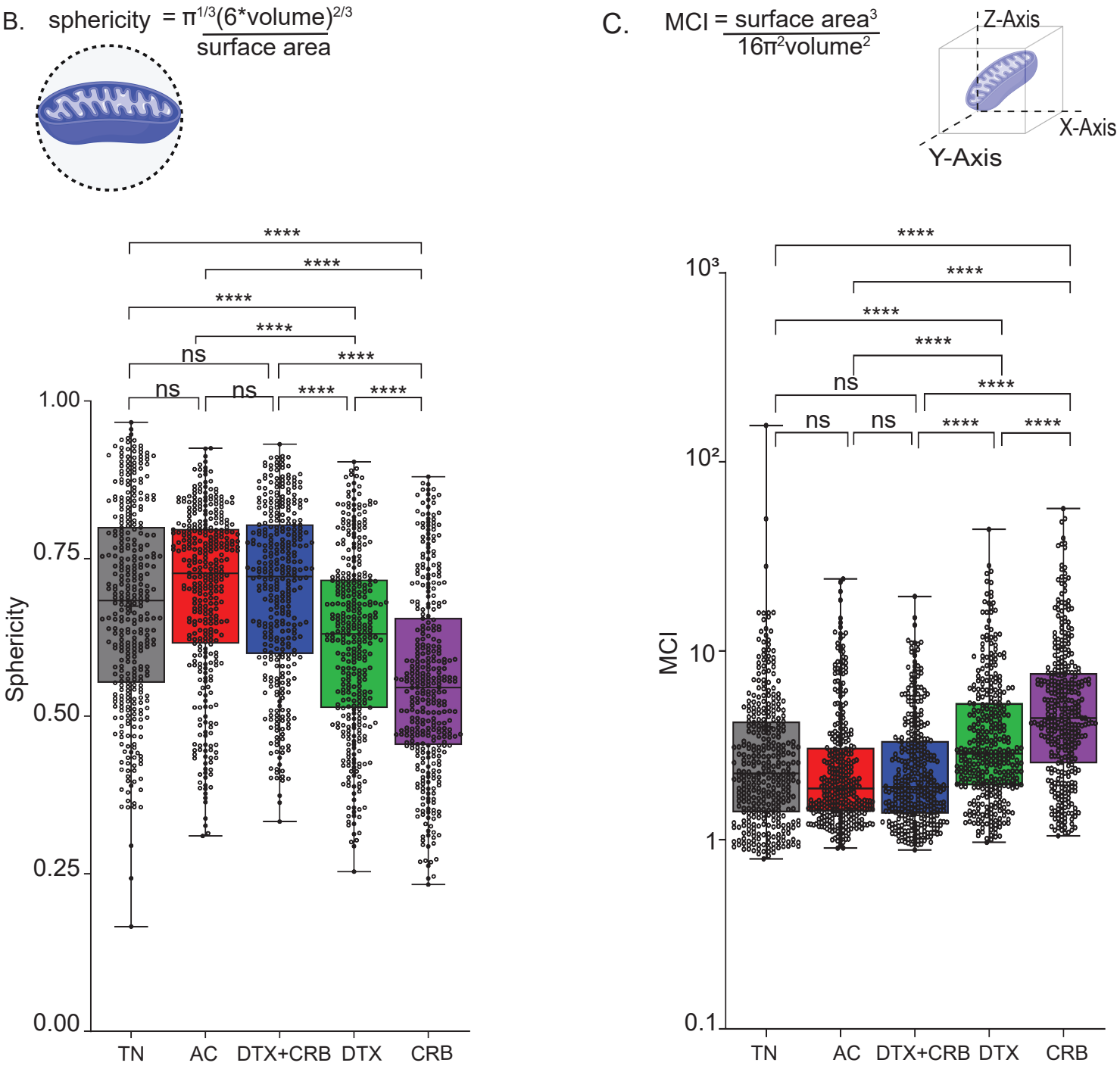

Figure 3. Single-agent chemotherapy treated residual tumors' mitochondria are more branched and less spherical relative to TN in PIM001-P.

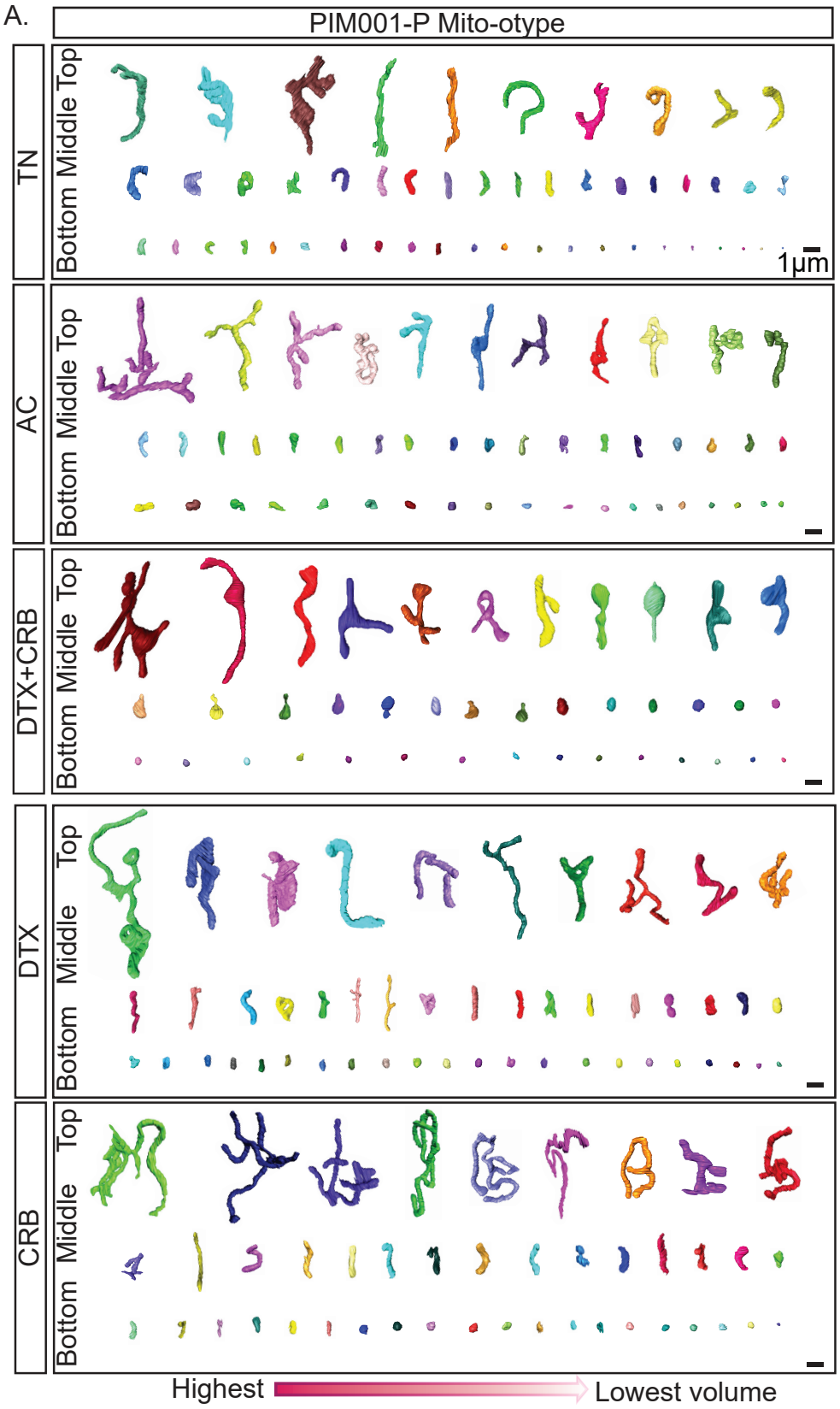

Figure 4. PIM001-P mito-otyping of the diverse mitochondrial structures observed within each treatment group.

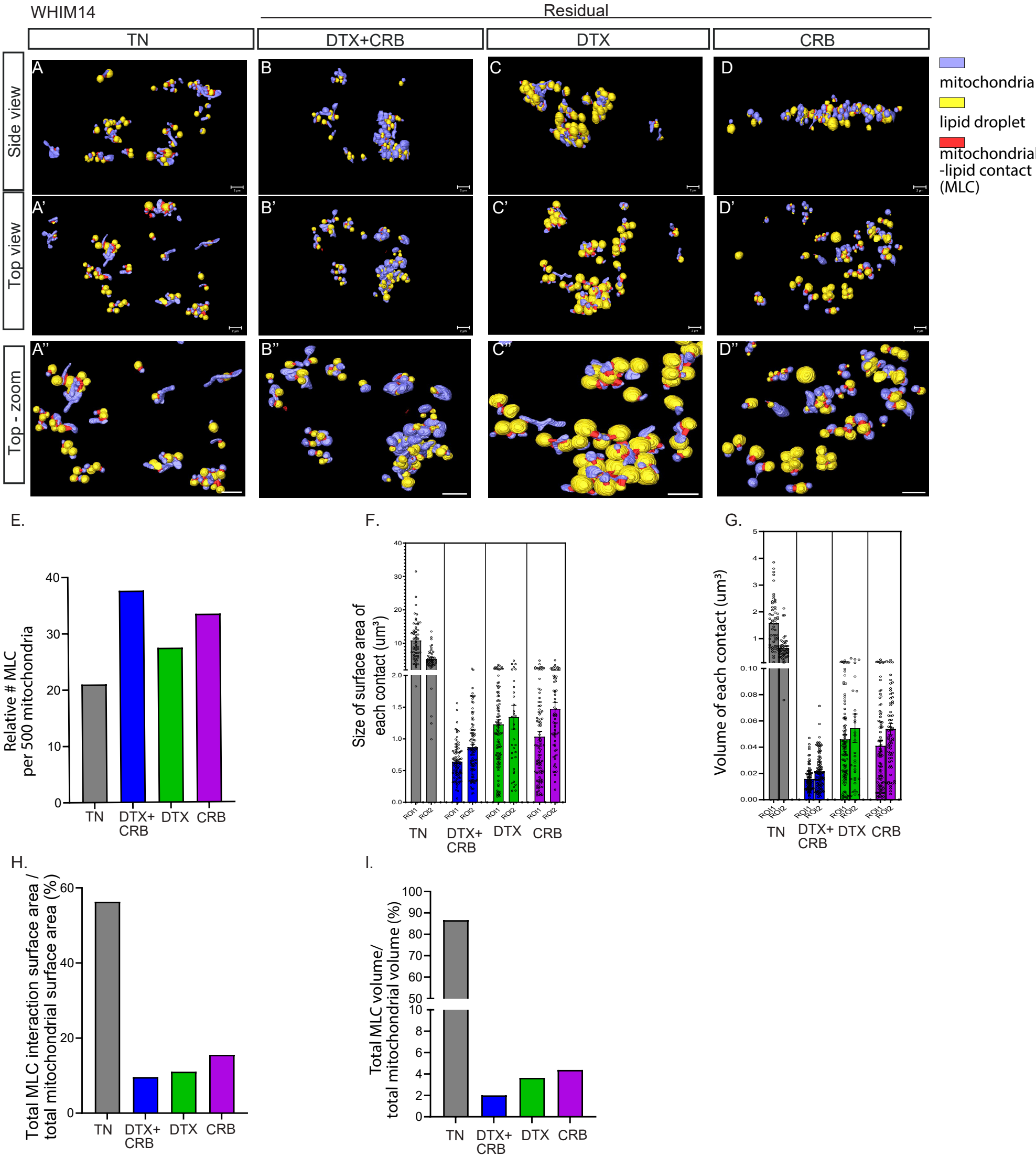

Figure 5. The frequency of MLCs increases upon chemotherapy, while the sizes of the contacts decrease in WHIM14.